1 **Aggravated surface O₃ pollution primarily driven by meteorological variation**

2 **in China during the 2020 COVID-19 pandemic lockdown period**

3

4 Zhendong Lu[1*], Jun Wang[1,2*], Yi Wang[2,3], Daven K. Henze[4], Xi Chen[2], Tong Sha[2,5], Kang Sun[6,7]

5

6 *[1]Interdisciplinary Graduate Program in Informatics, The University of Iowa, Iowa City, IA,*

7 *United States*

8 *[2]Department of Chemical and Biochemical Engineering, Center for Global and Regional*

9 *Environmental Research and Iowa Technology Institute, The University of Iowa, Iowa City, IA,*

10 *United States*

11 *[3]Now at Hubei Key Laboratory of Regional Ecology and Environmental Change, School of*

12 *Geography and Information Engineering, China University of Geosciences, Wuhan, China*

13 *[4]Department of Mechanical Engineering, University of Colorado, Boulder, CO, United States*

14 *[5]Now at School of Environmental Science and Engineering, Shaanxi University of Science and*

15 *Technology, Xi'an, China*

16 *[6]Department of Civil, Structural and Environmental Engineering, University at Buffalo, Buffalo,*

17 *NY, United States*

18 *[7]Research and Education in Energy, Environment and Water Institute, University at Buffalo,*

19 *Buffalo, NY, United States*

20

21 *Correspondence to: Jun Wang (jun-wang-1@uiowa.edu) and Zhendong Lu (zhendong-

22 lu@uiowa.edu)

23

26

Abstract

Due to the lockdown during the COVID-19 pandemic in China from late January to early April in 2020, a significant reduction of primary air pollutants, as compared to the same time period in 2019, has been identified by satellite and ground observations. However, this reduction is in contrast with the increase of surface O_3 concentration in many parts of China during the same period from 2019 to 2020. The reasons for this contrast are studied here from two perspectives: emission changes and inter-annual meteorological variations. Based on top-down constraints of NOx emissions from TROPOMI measurements and GEOS-Chem model simulations, our analysis reveals that NOx and volatile organic compound (VOC) emission reductions as well as meteorological variations lead to 8%, -3%, and 1% changes in O_3 over North China, respectively. In South China, however, we find that meteorological variations cause ~30% increases in O_3, which is much larger than -1% and 2% changes due to VOC and NOx emission reductions, respectively, and the overall O_3 increase in the simulations is consistent with the surface observations. The higher temperature associated with increase of solar radiation and declined relative humidity are the main reasons that lead to the surface O_3 increase in South China. Collectively, inter-annual meteorological variations have a larger impact than emission reductions on the aggravated surface O_3 pollution in China during the lockdown period of COVID-19 pandemic.

1. Introduction

Surface ozone (O_3), an important air pollutant that is harmful to human health (Jerrett et al., 2009) and stomatal conductance of green vegetations (Gong et al., 2020), is produced by photochemical reactions of nitrogen oxides (NOx) and volatile organic compounds (VOC) (Liu et al., 1987; Sillman et al., 1990). In addition to emissions, meteorological conditions, such as temperature, solar radiation and relative humidity, also have large impacts on surface O_3 formation (Lu et al., 2019).

Ground observations show that surface O_3 increased dramatically during the COVID-19 lockdown period in China by around 40% on average (Tong et al., 2023) and even larger than 100% (Shi and Brasseur, 2020; Liu et al., 2021) depending on the time period and region. The reduction of economic activities during the lockdown period led to a significant decrease of several primary air pollutants emissions. The NO_2 vertical column density (VCD) from satellite measurements and

58   surface NO$_2$ concentration from ground measurements were reduced by 40% - 60% in China

59   during the lockdown period (Bauwens et al., 2020; Shi and Brasseur, 2020; Liu et al., 2020a; Zhang

60   et al., 2020). A lower but discernible reduction of sulfur dioxide (SO$_2$), carbon monoxide (CO),

61   and formaldehyde (HCHO) have also been identified by satellite or ground-based observations in

62   China (Shi and Brasseur, 2020; Levelt et al., 2022; Ghahremanloo et al., 2021). However, during

63   this period surface O$_3$ concentrations increased, and the respective roles of meteorological factor

64   and emission reduction for the aggravated surface O$_3$ pollution during the lockdown in China need

65   to be further quantified.

66   This study provides a quantitative analysis of the causes for the unexpectedly aggravated

67   surface O$_3$ pollution in China during the lockdown period of the pandemic from two perspectives

68   using GEOS-Chem model. One is anthropogenic emission reduction of NOx and VOC in response

69   to the lockdown possibly under a VOC-limiting chemical regime of surface O$_3$ production (Guo

70   et al., 2023), while the other is the impact of natural variability of meteorological conditions.

71   Previous studies have reported the enhanced surface O$_3$ due to NOx emission decline during the

72   lockdown period in North China using chemical transport model (CTM) simulations without

73   controlling for the impacts of meteorological variability (Zhang et al., 2021; Huang et al., 2020;

74   Miyazaki et al., 2020). Other studies quantified or excluded the meteorological impacts on the

75   surface O$_3$ using statistical analysis instead of CTM that account for the physical and chemical

76   processes (Venter et al., 2020; Bi et al., 2022; Tong et al., 2023). Although a few studies have

77   investigated the contributions from both emission reduction and meteorological variability to

78   surface O$_3$ increase using CTMs, most of their results have uncertainties due to the limitations of

79   their analysis. For example, some of them keep the emissions unchanged (Zhao et al., 2020) or

80   assume an arbitrarily uniform emission reduction instead of constraining the emission based on

81   observations (Le et al., 2020; Liu et al., 2021). In cases where the emissions were constrained by

82   the observations, the focus was limited to several cities in China (Liu et al., 2020b). Furthermore,

83   in the past studies, the surface O$_3$ increase during the lockdown period of 2-4 weeks is quantified

84   in reference to the time period right before the lockdown instead of the same period in previous

85   years; such comparisons by design cannot exclude the possibility that the seasonal variation of

86   meteorology from early January to early April may have dominated the cause for the surface O$_3$

87   increase. A comprehensive analysis of the contributions from emission reductions and

88 meteorological variations to the surface O$_3$ increase during the first round of the lockdown period
89 with respect to the same time period in previous years in China is therefore overdue.

90   Here, we apply a top-down method to update NOx and VOC emission in February and
91 March in 2020 based on the TROPOMI NO$_2$ and formaldehyde (HCHO) product. A set of GEOS-
92 Chem model simulations with NOx and VOC emissions and meteorological fields in different time
93 periods are then conducted. Based on the difference in surface O$_3$ concentration in different
94 modeling sensitivity experiments, we quantitatively assess the respective roles of emission and
95 meteorology in regulating surface O$_3$ concentration in continental China. The ground observations
96 of surface O$_3$ and NO$_2$ concentration are compared with the model simulations to verify our
97 analysis. Section 2 introduces the satellite and ground-based measurements, NOx emission update
98 scheme, and the configurations of GEOS-Chem simulation experiments. Section 3 provides an
99 evaluation of the constrained NOx emission and surface O$_3$ simulations. The analysis of the
100 mechanism of the aggravated surface O$_3$ pollution is presented in Section 4, followed by the
101 summary and conclusions in Section 5.

102

103 2. Datasets and Methods

104 2.1 TROPOMI NO$_2$ and HCHO product

105   We used tropospheric NO$_2$ and HCHO level 2 VCD product provided by the Tropospheric
106 Monitoring Instrument (TROPOMI) onboard the Sentinel-5 Precursor (S5P) satellite (Veefkind et
107 al., 2012). S5P is a sun-synchronous polar orbit satellite launched on 13 October 2017, which
108 covers the near-global domain in a single day. TROPOMI provides NO$_2$ and HCHO retrievals at
109 an approximately 7 km x 3.5 km spatial resolution (5.5km x 3.5 km since 6 August 2019) from the
110 ascending orbit with an equatorial crossing time of ~13:30 local time (Van Geffen et al., 2020; De
111 Smedt et al., 2018). The datasets were obtained from the NASA Goddard Earth Sciences Data and
112 Information Services Center (https://daac.gsfc.nasa.gov). A quality control procedure similar to
113 Bauwens et al. (2020) but with slightly stricter criteria is adopted for TROPOMI NO$_2$ and HCHO
114 data. The TROPOMI retrievals under one or more than one of the following conditions are
115 screened out for data quality control. (1) Quality assurance value is no larger than 0.5; (2) cloud
116 radiance fraction within NO$_2$ or HCHO retrieval window is larger than 0.3; (3) solar zenith angle
117 is larger than 70°; and (4) viewing zenith angle is larger than 70°.

118

2.2 Ground O_3 and NO_2 measurements

Surface measurements of O_3 and NO_2 were collected from ~1600 operational air quality monitoring stations over the mainland China managed by the China National Environmental Monitoring Center (http://www.cnemc.cn/en/). We calculated daily maximum 8-hour average (MDA8) O_3 concentration from hourly in situ measurements. Surface O_3 are measured by ultraviolet photometric method and Indigo disulfonate spectrophotometry, following the national environmental standards of HJ 590-2010 and HJ 504-2009. Surface NO_2 concentrations are measured by the chemiluminescence method (Zhang and Cao, 2015) that quantifies the NO_2 concentrations by measuring the NO decomposed from NO_2, which can cause a positive bias in the NO_2 measurements (Steinbacher et al., 2007) because NOz (compounds produced from the atmospheric oxidation of NOx) can also be decomposed to NO. The true NO_2 concentrations only account for 43%‐76% and 70%‐83% of measured values for rural and urban sites (Steinbacher et al., 2007). Following Wang et al. (2020b), we also applied a correction factor but with a lower value of 0.75 to the measured NO_2, considering that we included both rural and urban sites. The sampling ports are placed at 3 to 15 meters above the ground following the national environmental monitoring method standard HJ 664-2013. The measured data are reported in the unit of $\mu g\ m^{-3}$ under standard temperature (273.15 K) and pressure (101.325 kPa) according to national environmental standards GB 3095-2012.

2.3 GEOS-Chem model and its adjoint

The global 3-D chemical transport model GEOS-Chem (Bey et al., 2001) version 12.7.2 is used here. We apply the nested-grid version of GEOS-Chem (Chen et al., 2009; Wang et al., 2004) with the horizontal resolution of 0.25°×0.3125° and 47 vertical hybrid-sigma levels over East Asia (70°E-140°E, 15°N-55°N). The boundary conditions are obtained from the 2°×2.5° global simulation. The model is driven by the GEOS-FP meteorological field provided by NASA Global Modeling and Assimilation Office (GMAO). A detailed O_3-NOx-hydrocarbon chemistry (Mao et al., 2010; Mao et al., 2013; Travis et al., 2016) is included in the GEOS-Chem model. The altitude of the surface O_3 output from GEOS-Chem is specified at 9 meters above the ground to match the in-situ measurements (Travis et al., 2017; Zhang et al., 2012). Through our sensitivity test using GEOS-Chem, the variation of surface O_3 from 3 to 9 meters above the surface is generally less than 0.723 ppb (75th percentile), and the median bias is 0.283 ppb. Travis et al. (2017) reported

150   from 60 m to 10 m above the ground, the MDA8 O_3 could decrease by ~3 ppb. Therefore, when

151   comparing GEOS-Chem surface O3 with in-situ measurements, the differences caused by

152   inconsistent reported altitudes (9 m versus 3-15 m) can be ignored.

153   The global anthropogenic emission used in GEOS-Chem model is the Community

154   Emissions Data System (CEDS) inventory (Hoesly et al., 2018), which is replaced by the MIX

155   inventory (Li et al., 2017) over the Asian region. Biogenic emissions for VOCs follows the Model

156   of Emissions of Gases and Aerosols from Nature (MEGAN) inventory (Guenther et al., 2012).

157   Natural NOx emissions includes biomass burning from GFED4 inventory (Van Der Werf et al.,

158   2017), soil NOx emissions (Hudman et al., 2012) and lightning sources (Murray et al., 2012; Ott

159   et al., 2010).

160   The adjoint of the GEOS-Chem model (Henze et al., 2007; Henze et al., 2009) is a

161   component of the 4D-Var inversion method that can efficiently optimize spatially disaggregated

162   aerosol and gas emissions. This is done through iterative minimization of a cost function using the

163   model adjoint to calculate the gradient of the cost function with respect to a large number of model

164   parameters (such as anthropogenic NOx emissions in each grid box) simultaneously. The cost

165   function is the sum of the error weighted difference between forward model outputs and

166   observations and the divergence of posterior model parameters from the prior estimate (Section

167   2.4). We developed and validated the observation operator for TROPOMI NO_2 in the GEOS-Chem

168   adjoint model version 35n similar to Wang et al. (2020a) and used it to optimize the anthropogenic

169   NOx emission during the lockdown period in China. The monthly NOx emission optimization is

170   implemented using the 4D-Var method with GEOS-Chem adjoint at the nested grid with the

171   resolution of 0.25°×0.3125° via assimilating the daily TROPOMI NO_2 measurements. The prior

172   anthropogenic NOx emission used in the GEOS-Chem adjoint is HTAP version 2 (Janssens-

173   Maenhout et al., 2015), which is equivalent to the MIX inventory in East Asia (Li et al., 2017).

174

175   **2.4 NOx and VOC emission updates**

176   Two approaches are used to update the emissions during the lockdown period in 2020. The

177   first is a simple mass balance approach (Leue et al., 2001; Martin et al., 2003; Vinken et al., 2014)

178   for updating the NOx emission by assuming a constant NOx lifetime and NOx/NO_2 ratio. In the

179   period from 2010 to 2019, the anthropogenic NOx emissions have declined significantly as a result

180   of the clean air actions of Chinese government (Zheng et al., 2018). We scale the anthropogenic

181 NOx emission from year 2010 to 2019 using the spatially gridded ratio of mean TROPOMI
182 tropospheric NO_2 VCD in Feb.-Mar. 2019 to GEOS-Chem simulated NO_2 column with default
183 MIX 2010 emission (Appendix A), to obtain the baseline anthropogenic NOx emission in 2019,
184 which is denoted as MIX 2019. To derive anthropogenic NOx emissions in 2020 in China during
185 the COVID-19 lockdown (MIX 2020), the spatially gridded ratio of mean TROPOMI tropospheric
186 NO_2 VCD in 2020 Feb.-Mar. to that in 2019 Feb.-Mar. is taken as a scaling factor for the updated
187 baseline anthropogenic NOx emission in 2019 (MIX 2019). The two-month mean of TROPOMI
188 NO_2 VCD in 2019 and 2020 are calculated with the physical oversampling procedure (Sun et al.,
189 2018). Scaling factors in regions where mean TROPOMI tropospheric NO_2 VCD in 2019 Feb.-
190 Mar. is less than 0.1 Dobson unit (DU) are set to 1 for emission updates in both 2020 and 2019,
191 assuming that the lockdown only affects the populated areas (that have high NO_2 in 2019).

192   The second method for updating NOx emission is 4D-Var via the GEOS-Chem adjoint
193 model. The anthropogenic NOx emissions in 2020 lockdown period derived from the GEOS-Chem
194 adjoint is denoted as 2020 Adjoint. Following Wang et al. (2020a), the cost function J for
195 optimizing the NOx emission is defined as

$$J = \frac{1}{2}\sum_{c\in\Omega}[H(\boldsymbol{c}) - \boldsymbol{s}]^{\mathrm{T}}\boldsymbol{S}_{\mathrm{obs}}^{-1}[H(\boldsymbol{c}) - \boldsymbol{s}] + \frac{1}{2}\gamma(\boldsymbol{\sigma} - \boldsymbol{\sigma}_a)^{\mathrm{T}}\boldsymbol{S}_a^{-1}(\boldsymbol{\sigma} - \boldsymbol{\sigma}_a) \qquad (1)$$

197 where $\boldsymbol{s}$ is the tropospheric slant column density of TROPOMI NO_2, which is the product of
198 TROPOMI NO_2 VCD and air mass factor. H is the TROPOMI NO_2 observation operator that maps
199 the modeled NO_2 concentrations $\boldsymbol{c}$ to the observations in time and space and calculates the
200 corresponding slant column density to make an apple-to-apple comparison of the model to
201 TROPOMI. Ω is the spatial and temporal domain where both model simulations and observations
202 are available. $\boldsymbol{\sigma}$ is the scaling factor of anthropogenic NOx emissions to be optimized, and $\boldsymbol{\sigma}_a$ is
203 the prior emission scaling factors, which equals 1. $\boldsymbol{S}_{\mathrm{obs}}$ and $\boldsymbol{S}_a$ are observational and prior error
204 covariance matrices, respectively. γ is the regularization factor that balances the weights of the
205 observational term and prior term. We assumed $\boldsymbol{S}_{\mathrm{obs}}$ to be diagonal following Wang et al. (2020a)
206 with the diagonal values calculated as the square of the standard error of tropospheric NO_2 slant
207 column density from the TROPOMI product. The prior error of the NOx emissions is assumed to
208 be 100%. The spatial correlation of NOx emissions is considered in this study, and the off-diagonal
209 elements of $\boldsymbol{S}_a$ are computed by assuming an exponentially decaying error correlation with a fixed

210   decaying distance of 150 km following Qu et al. (2017). The γ value was determined as 500 via

211   the total error minimization and L-curve test (Henze et al., 2009; Qu et al., 2017).

212   We developed the observation operator for TROPOMI NO_2 product in the GEOS-Chem

213   adjoint model with GEOS-Chem NO_2 vertical profiles and TROPOMI NO_2 averaging kernel

214   applied to minimize the discrepancies between the assumptions in TROPOMI NO_2 retrieval and

215   GEOS-Chem model simulation. See Appendix B for additional details. The observation operator

216   has been validated using the finite difference method (Appendix C).

217   For anthropogenic VOC emissions update, we only applied the mass balance method based

218   on the TROPOMI HCHO data. The default anthropogenic VOC emissions used in the GEOS-

219   Chem is also MIX 2010 (Li et al., 2017). We ignore the change of anthropogenic VOC emissions

220   from 2010 to 2019 (Appendix D). The baseline VOC emission in 2019 (MIX 2019) is identical to

221   that of MIX 2010. The updated anthropogenic VOC emissions during the lockdown period is

222   denoted as MIX 2020. HCHO is one species of VOC and may not be able to represent other VOC

223   species. Different from NOx, biogenic sources, meteorological impacts, and large retrieval

224   uncertainty of HCHO due to its low optical depth prevent accurately quantifying the emission

225   decline due to lockdown from satellite retrievals (Levelt et al., 2022). Vigouroux et al. (2020)

226   reported that TROPOMI HCHO tends to be overestimated by ~26% for HCHO column lower than

227   2.5×10^{15} molecules cm^{-2} and underestimated by ~31% for HCHO column higher than 8.0×10^{15}

228   molecules cm^{-2}. To optimize the signal, we spatially aggregate the ratio of TROPOMI HCHO in

229   2020 Feb.-Mar. to that in 2019 Feb.-Mar. to the resolution of 0.5°, which are used as the scaling

230   factors for updating the anthropogenic VOC emissions during the lockdown period. The

231   aggregation is based on the oversampling of TROPOMI HCHO at 0.01° resolution, and the ratio

232   is computed as the mean of the lowest 25th percentile of all ratios at 0.01° resolution in each

233   0.5°×0.5° grid box, which ensures that only statistically significant changes are considered. We

234   assumed the change of anthropogenic VOC emissions over sparsely populated areas (TROPOMI

235   NO_2 in 2019 Feb.-Mar. less than 0.1 DU) is insignificant and assigned the ratio values as one. To

236   further evaluate the uncertainties associated with this approach, we also conducted sensitivity

237   study by using different threshold in the aggregation.

238   We assess the results from model experiments (as described in Section 2.5) adopting the

239   updated NOx emission by comparing mean tropospheric NO_2 VCD from GEOS-Chem and from

240   TROPOMI observations in Feb.-Mar. of 2019 and 2020. The averaging kernel of TROPOMI NO_2

241 is applied to modeled NO$_2$ column for this comparison, following Sha et al. (2021). Further
242 quantitative evaluation of the model results also used the TROPOMI measurements of HCHO and
243 surface observation of O$_3$ and NO$_2$.

244

245 **2.5 GEOS-Chem model experiments**

246   A series of sensitivity experiments is conducted over China with different NOx and VOC
247 emissions and GEOS-FP meteorological fields in different years using GEOS-Chem (v12.7.2)
248 model. All simulations are conducted from Jan. 15 to Mar. 31. The 17 days before Feb. 1 are used
249 for spin up, and the model output for Feb. and Mar. are used for the analysis. The configurations
250 of different simulations are listed in Table 1.

251

252 **Table 1.** Configurations of model sensitivity experiments.

Experiments	Abbreviation	Meteorology	NOx Emission	VOC Emission
Baseline (2019)	2019B	GEOS-FP 2019	MIX 2019	MIX 2019
2020 Default	2020D	GEOS-FP 2020	MIX 2019	MIX 2019
2020 NOx	2020N	GEOS-FP 2020	MIX 2020	MIX 2019
2020 VOC	2020V	GEOS-FP 2020	MIX 2019	MIX 2020
2020 Lockdown	2020L	GEOS-FP 2020	MIX 2020	MIX 2020
2020 Adjoint	2020A	GEOS-FP 2020	Adjoint 2020	MIX 2020

253

254   We use the following equations to quantify the contributions from NOx and VOC emission
255 reduction due to COVID-19 and meteorological variation to the increase of surface O$_3$.

$$\Delta O_3^{\text{NOx}} = \frac{O_3^{2020\text{A}} - O_3^{2020\text{V}}}{O_3^{2019\text{B}}} \times 100\% \tag{2}$$

$$\Delta O_3^{\text{VOC}} = \frac{O_3^{2020\text{L}} - O_3^{2020\text{N}}}{O_3^{2019\text{B}}} \times 100\% \tag{3}$$

$$\Delta O_3^{\text{ems}} = \frac{O_3^{2020\text{A}} - O_3^{2020\text{D}}}{O_3^{2019\text{B}}} \times 100\% \tag{4}$$

$$\Delta O_3^{\text{met}} = \frac{O_3^{2020\text{D}} - O_3^{2019\text{B}}}{O_3^{2019\text{B}}} \times 100\% \tag{5}$$

260   Where ΔO_3^{NOx}, ΔO_3^{VOC} and ΔO_3^{ems} are the relative differences in surface O3 concentration caused

261   by emission decline of NOx, VOC, and both NOx and VOC resulting from COVID-19. ΔO_3^{met}

262   represents the relative contribution to the surface O3 change from the meteorological variation

263   between 2 years. O_3^{2019B}, O_3^{2020D}, O_3^{2020N}, O_3^{2020V}, O_3^{2020L} and O_3^{2020A} are mean MDA8 surface

264   O3 concentration simulated by modeling experiments Baseline (2019), 2020 Default, 2020 NOx,

265   2020 VOC, 2020 Lockdown and 2020 Adjoint, respectively (Table 1).

266   The difference in simulated surface O3 between 2020 and 2019, is the result of both

267   emission reductions and meteorological variations and is denoted as ΔO_3^{all}. It is calculated as

268   follows and is evaluated against the observed relative difference of mean MDA8 O3 in Feb. to Mar.

269   between 2019 and 2020 at all ground sites:

270
$$\Delta O_3^{all} = \frac{O_3^{2020A} - O_3^{2019B}}{O_3^{2019B}} \times 100\% \tag{6}$$

271

## 272   3. Results of model development, emissions, and validation

273   3.1 Changes of NOx and VOC emissions during COVID

274   We updated the anthropogenic NOx emissions during the COVID lockdown using both

275   4D-Var and mass balance methods (Fig. 1 and 2). The NOx emissions from the 4D-Var inversion

276   share a similar spatial pattern and magnitude with those found using the mass balance method (Fig.

277   1). However, the NOx emissions from the 4D-Var inversion are lower overall than those from the

278   mass balance method over North China by ~10% and larger over central China by ~40%. Fig. 2(a-

279   b) shows that the 4D-Var NOx emission reduction is more severe over urban regions and displays

280   a smoother spatial pattern than that from the mass balance approach, which is caused by the

281   arbitrary cut off with 0.1 DU of NO2 VCD in the latter. Furthermore, the 4D-Var inversion

282   captured the NOx emission decline in Northeast China where the mass balance approach did not

283   because of the low NO2 VCD. During Feb.-Mar. 2020, the anthropogenic NOx emissions in East

284   China decreased by ~30% compared to those in the same period in 2019.

285   We also scale the anthropogenic VOC emissions based on the TROPOMI HCHO data (Fig.

286   2(c)). The VOC emissions decrease by ~20%-30% in East and South Asia. The anthropogenic

287   VOC emission changes in sparsely populated areas over Northwest China are neglected.

288   TROPOMI HCHO data cannot distinguish the anthropogenic emissions from biogenic and

289   biomass burning sources for the Indochinese Peninsula in Southeast Asia because of the dense

vegetation in this region. However, this study investigated the O_3 pollution in China, the Southeast Asia with the dense vegetation is out of our study domain. The impact of VOC emission bias in Southeast Asia on the surface O_3 pollution in China is negligible considering the lifetime of biogenic VOC is generally short (Atkinson, 2000). For the populated urban regions in China, where the surface O_3 pollution exerts more significant health impacts, the anthropogenic source dominates the VOC emissions (Williams and Koppmann, 2007).
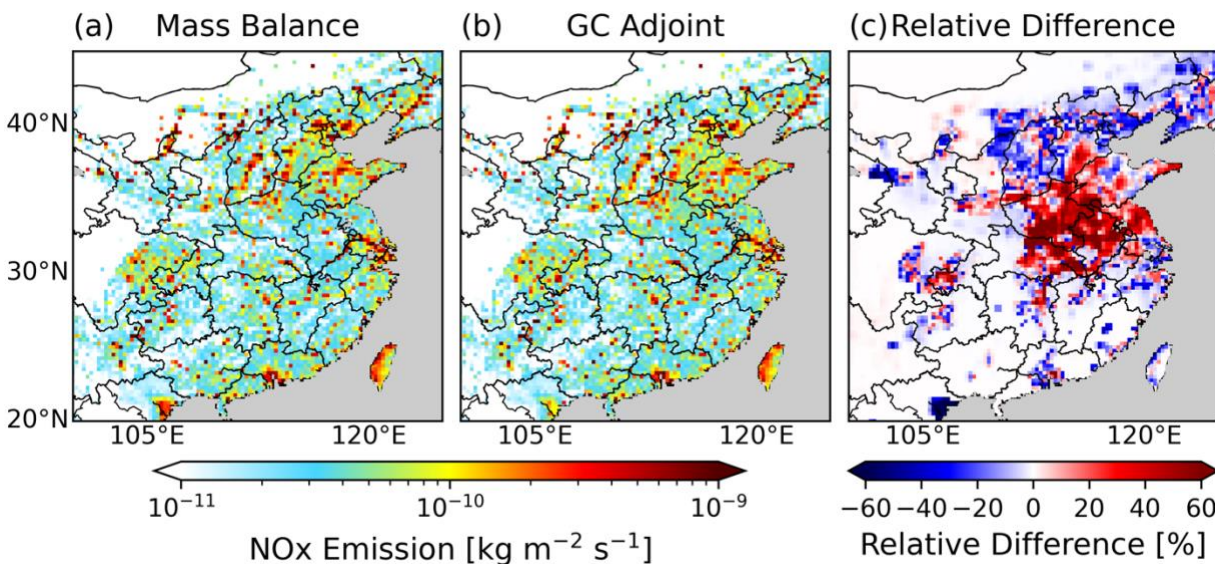
Figure 1. Updated anthropogenic NOx emission during Feb.-Mar. 2020 from (a) mass balance method, (b) 4D-Var method and (c) their relative difference. The relative difference is calculated as dividing the difference of (b) minus (a) by (a).
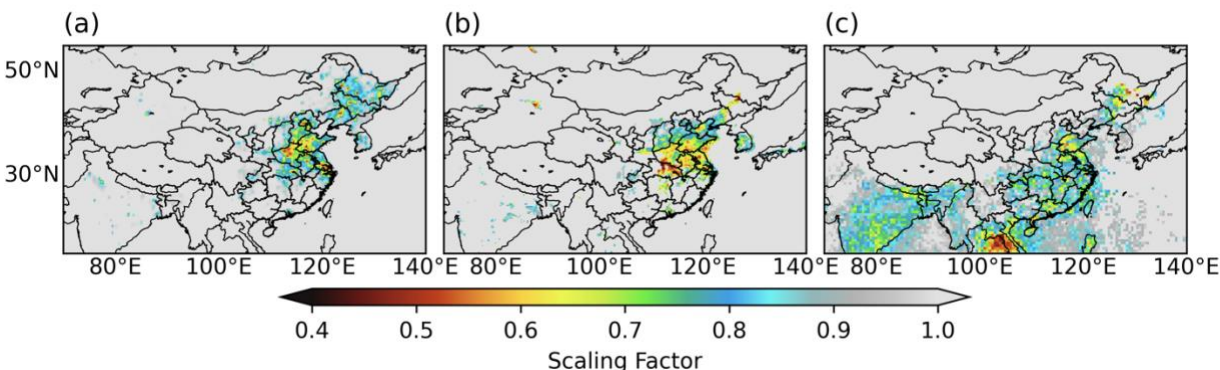

Figure 2. Scaling factors for anthropogenic NOx emission in Feb.-Mar. from 2019 to 2020 as derived from (a) 4D-Var, (b) mass balance. Scaling factors for anthropogenic VOC emissions from the mass balance are in (c).

11

3.2 Validation of NO$_2$ simulations

We further assess our updated anthropogenic NOx emissions by comparing the NO$_2$ VCD from TROPOMI with that from GEOS-Chem with the anthropogenic NOx emissions before and after the scaling (Fig. 3 and 4). Before updating the NOx emissions, the 2020 Default (Fig. 3(b)) simulation significantly overestimates the NO$_2$ VCD compared to the TROPOMI NO$_2$ observations (Fig. 3(a)). With the NOx emissions updated, the simulations 2020 NOx (Fig. 3(c)) and 2020 Adjoint (Fig. 3(d)) exhibit a much better agreement with TROPOMI NO$_2$ observation than 2020 Default. However, Fig. 3(c) shows the GEOS-Chem simulation with the NOx emissions from mass balance approach overestimated the NO$_2$ VCD over Beijing and southwest of Hebei Province (pink and black circles in Fig.3) compared with TROPOMI data. The reason is that scaling factors are applied only to anthropogenic NOx emissions, not total NOx emissions, so it is expected that the model may still overestimate the NO$_2$ column after scaling part of the total NOx emission. With the anthropogenic NOx emissions optimized by the 4D-Var method, the overestimation of NO$_2$ VCD over Beijing and southwest of Hebei Province (pink and black circles in Fig. 3) is mitigated compared with the NOx emissions from mass balance approach.

Fig. 4 further displays the statistics for the comparison between the TROPOMI NO$_2$ and GEOS-Chem simulations via the scatterplot. The Baseline (2019) simulation captures the magnitude of NO$_2$ VCD observations in 2019 well (Fig. 4(a)). The root-mean-square-error (RMSE) and mean bias error (MBE) for the simulation with 2020 NOx emission derived from mass balance method (Fig. 4(b)) decreased by 0.050 DU and 0.057 DU as compared to the 2020 Default (Fig. 4(c)). Compared with the result from GEOS-Chem simulation 2020 NOx, emissions from 2020 Adjoint (Fig. 4(d)) further led to the reduction of the MBE of the NO$_2$ VCD by 0.006 DU and improve the correlation coefficient by 0.003. The significant overestimation of several pixels with TROPOMI NO$_2$ VCD larger than 0.4 DU by the simulation 2020 NOx is also mitigated by 2020 Adjoint. The MBE between GEOS-Chem and TROPOMI for Baseline (2019), 2020 NOx and 2020 Adjoint are -0.004, 0.015 and 0.009 DU, respectively. The corresponding relative bias are 1.9%, 10% and 6.0%, which are all less than the relative uncertainty of ~30% for TROPOMI tropospheric NO$_2$ VCD over East China (Van Geffen et al., 2022). The improved agreement between the simulation with updated NOx emission and TROPOMI NO$_2$ provides a basis for further analyzing the mechanism of aggravated surface O$_3$ pollution.
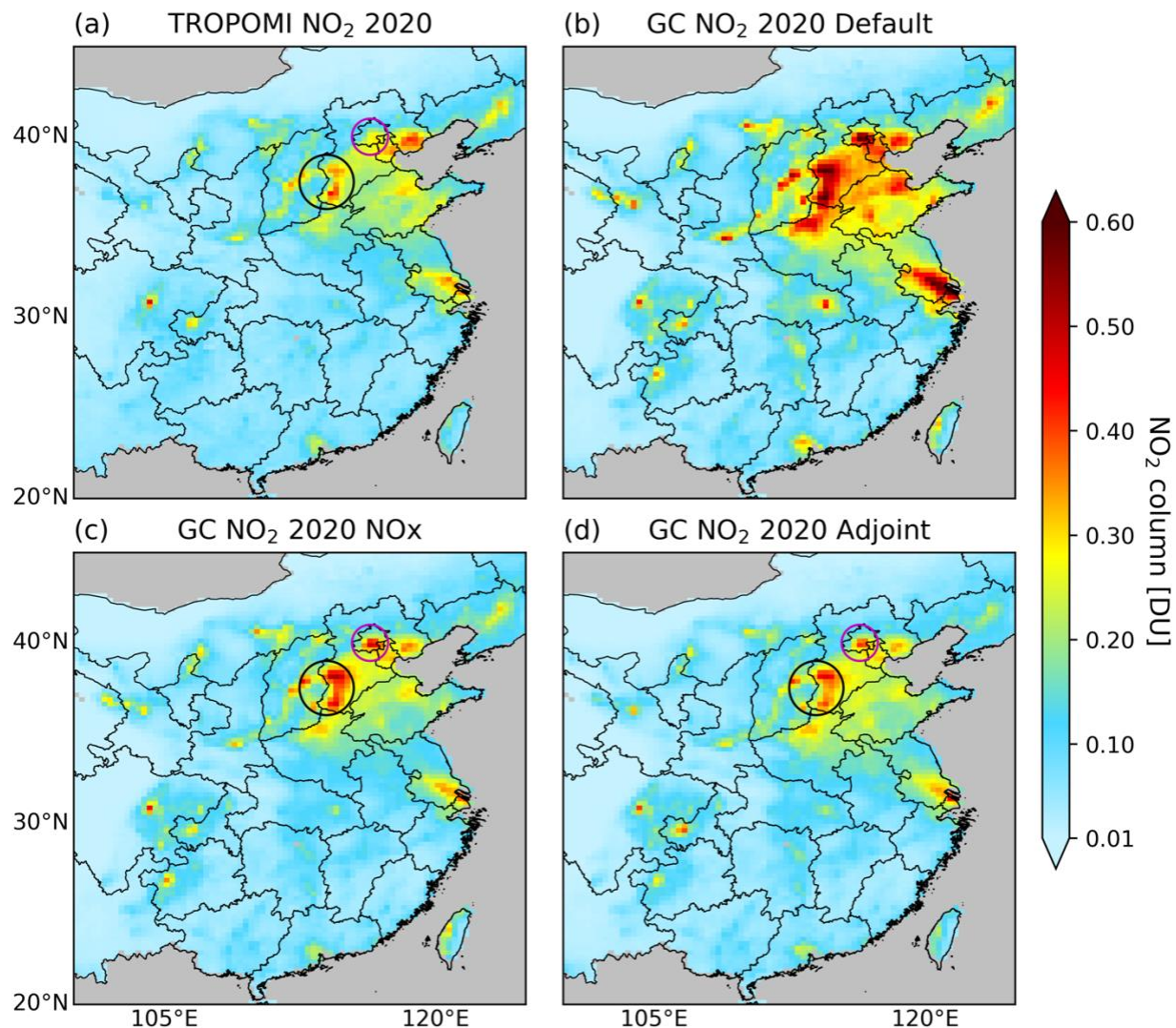
Figure 3. Comparison of tropospheric NO₂ VCD from (a) TROPOMI product in 2020 Feb.-Mar with that from GEOS-Chem simulations (b) 2020 Default, (c) 2020 NOx and (d) 2020 Adjoint. The pink and black circles mark the areas where NOx emissions from 4D-Var mitigated the NO₂ overestimation by mass balance method. The emissions and meteorology configurations for GEOS-Chem simulations 2020 Default, 2020 NOx and 2020 Adjoint are listed in Table 1.
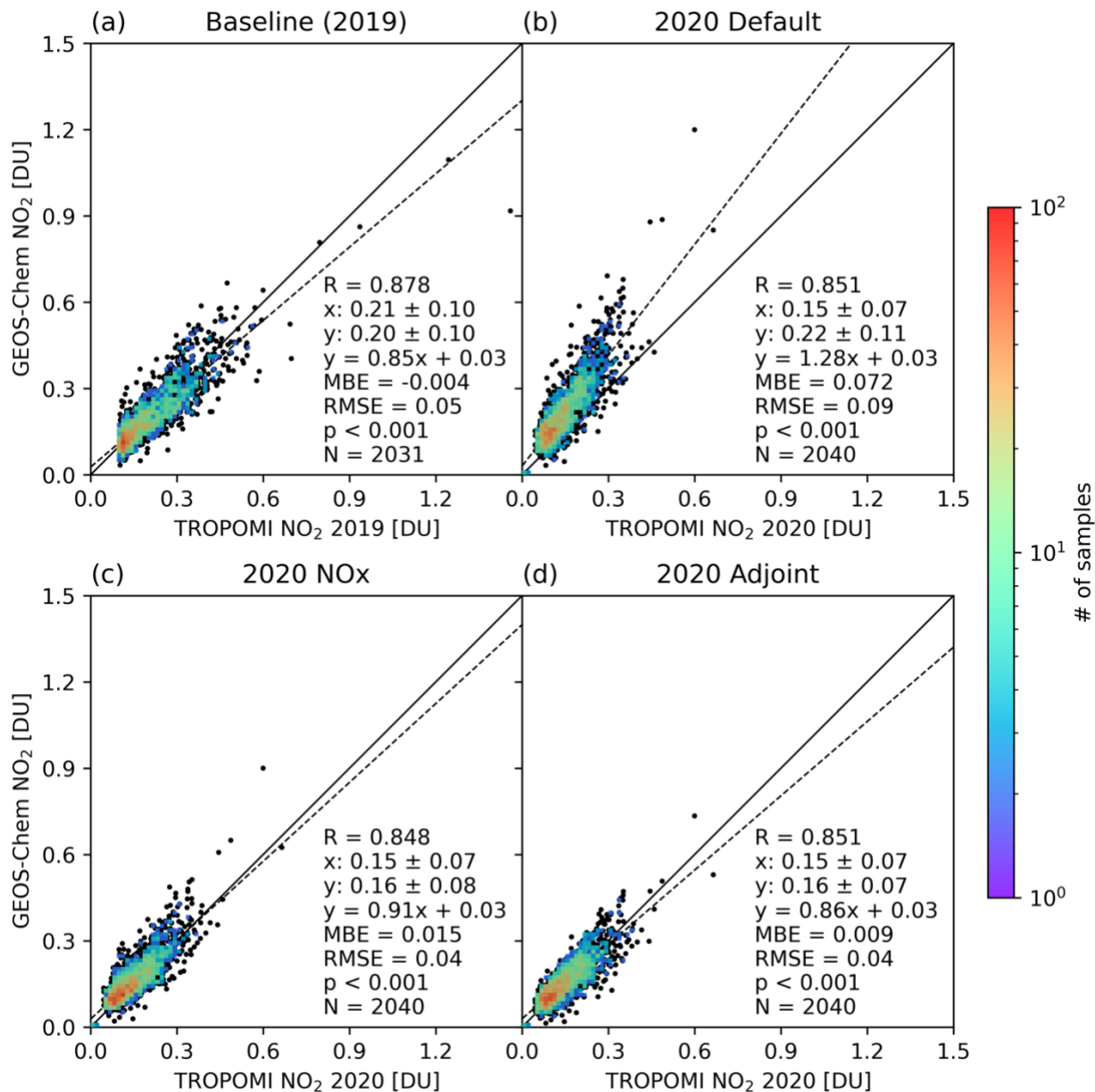
Figure 4. Scatter plot of TROPOMI NO$_2$ VCD versus the GEOS-Chem simulations for (a) Baseline (2019), (b) 2020 Default, (c) 2020 NOx and (d) 2020 Adjoint, respectively. TROPOMI data in Feb.-Mar. of 2019 was used in (a), and that of 2020 was used in (b-d). The emissions and meteorology configurations for GEOS-Chem simulations are listed in Table 1. Only pixels with TROPOMI NO$_2$ VCD in 2019 Feb.-Mar. larger than 0.1 DU are included in all comparisons.

351   Fig. 5 and Fig. 6 show the comparison of surface NO_2 between ground measurements and

352   GEOS-Chem simulations. The GEOS-Chem simulations Baseline (2019) (Fig. 5(b)) and 2020

353   Adjoint (Fig. 5(d)) both capture the spatial pattern and magnitude of surface NO_2 measurements

354   in Feb.-Mar. of 2019 (Fig. 5(a)) and 2020 (Fig. 5(c)) well, respectively. Fig. 6 further displays the

355   good agreements of surface NO_2 from Baseline (2019) (Fig. 6(a)) and 2020 Adjoint (Fig. 6(b)) to

356   the in-situ measurements via scatter plots. Table 2 displays the evaluation statistics, including the

357   correlation coefficient (R), MBE, RMSE and the slope and intercept of the linear regression, for

358   the simulated surface NO_2 from various simulation experiments compared with the in-situ

359   measurements. The correlation coefficient, MBE and RMSE between the simulation Baseline

360   (2019) and ground measurements in 2019 Feb.-Mar. are 0.724, 1.572 µg m^{-3} and 8.49 µg m^{-3},

361   respectively. Without updating the NOx emissions in 2020, the simulation 2020 Default

362   overestimate the ground measurements of surface NO_2 in 2020 Feb.-Mar (Table 2). The slope for

363   the linear regression is 1.19, and the MBE and RMSE are 6.021 µg m^{-3} and 10.43 µg m^{-3},

364   respectively (Table 2). After updating the NOx emissions, the GEOS-Chem simulations 2020 NOx

365   and 2020 Adjoint have good agreements with the in-situ measurements in 2020 Feb.-Mar. The

366   correlation coefficient between the simulation 2020 Adjoint versus the in-situ measurements is

367   0.651, higher than that of 0.608 for the simulation 2020 NOx versus the ground measurements

368   (Table 2). The MBE and RMSE of 2020 Adjoint (0.683 µg m^{-3} and 6.68 µg m^{-3}) are lower than

369   those of 2020 NOx (1.726 µg m^{-3} and 7.74 µg m^{-3}) (Table 2). This result further indicates the

370   superiority of 4D-Var for optimizing NOx emissions compared with the mass balance method

371   (Cooper et al., 2017; Streets et al., 2013).

372
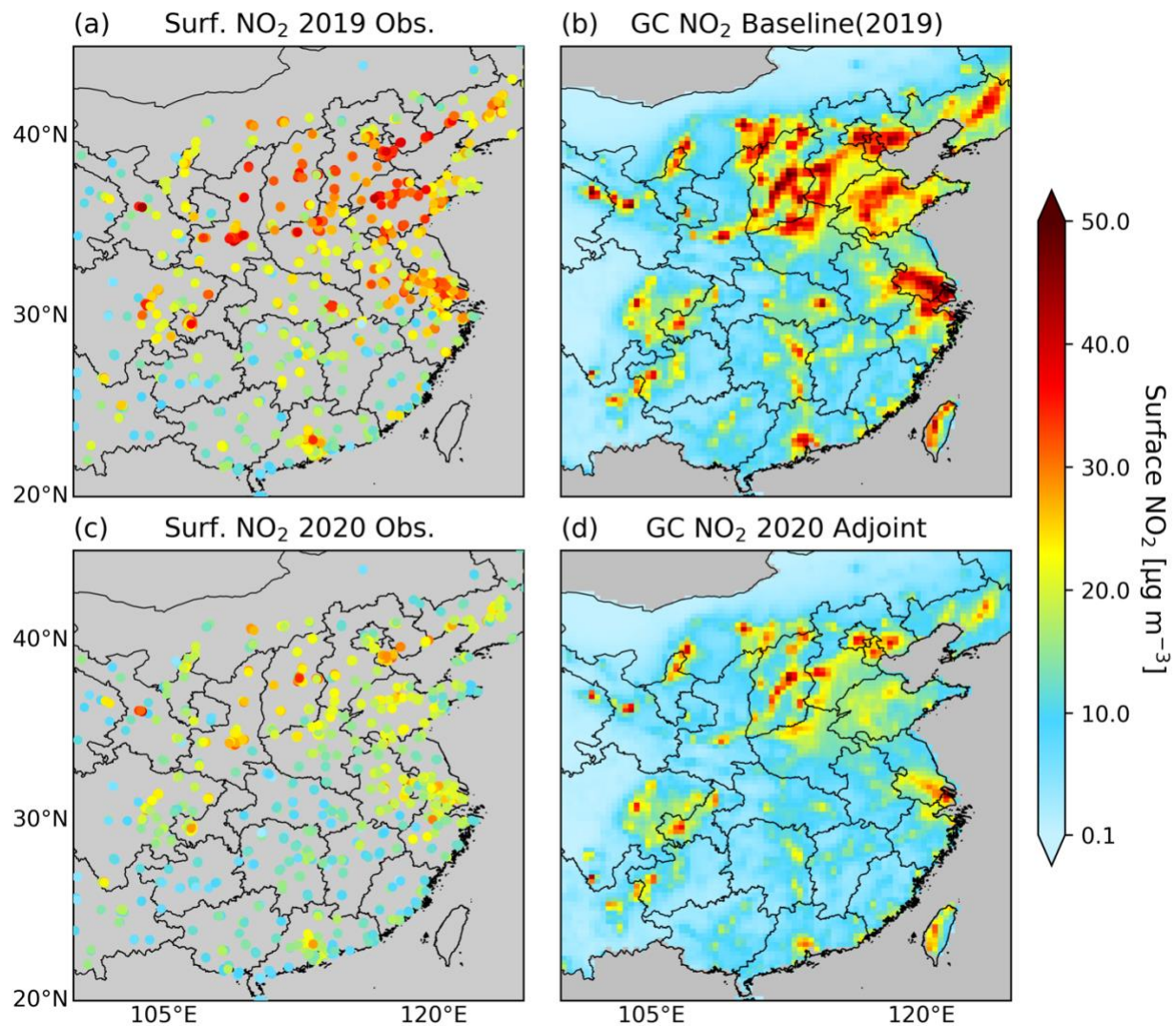
Figure 5. Comparison of surface NO₂ concentrations from ground measurements for (a) 2019 Feb.-Mar. and (c) 2020 Feb.-Mar. versus those from GEOS-Chem simulations (b) Baseline (2019) and (d) 2020 Adjoint. Grey color means no data is presented.
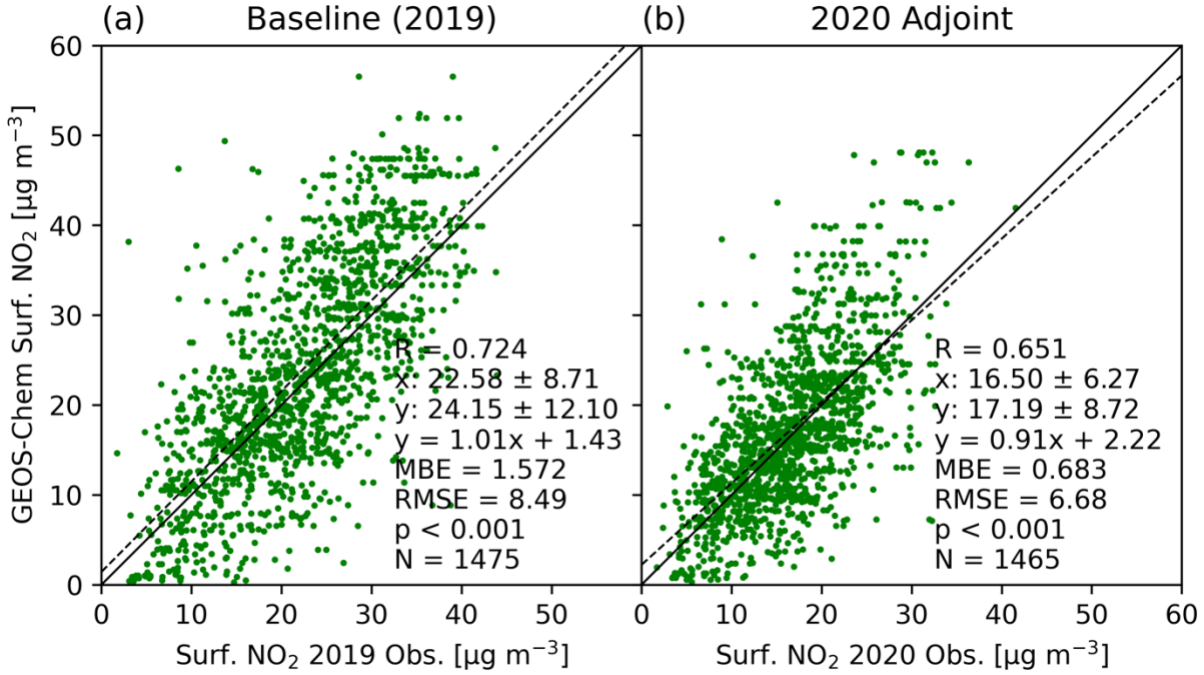
Figure 6. Scatter plots for comparing the surface NO_2 concentrations from GEOS-Chem simulations and ground measurements. (a) GEOS-Chem simulation Baseline (2019) versus ground measurements in 2019 Feb.-Mar. (b) GEOS-Chem simulation 2020 Adjoint versus ground measurements in 2020 Feb.-Mar. Note: the number of ground sites differ in these two years.

Table 2. Evaluation statistics for modeled surface NO_2 compared with the in-situ measurements*.

Experiments	R	MBE ($\mu g\ m^{-3}$)	RMSE ($\mu g\ m^{-3}$)	Slope	Intercept ($\mu g\ m^{-3}$)
Baseline (2019)	0.724	1.572	8.49	1.01	1.43
2020 Default	0.661	6.021	10.43	1.19	2.95
2020 NOx	0.608	1.726	7.74	0.92	3.03
2020 Adjoint	0.651	0.683	6.68	0.91	2.22

* The simulation experiment Baseline (2019) is compared with the ground measurements in 2019 Feb.-Mar. Other three experiments are compared with the ground measurements in 2020 Feb.-Mar.

Fig. 7 (a) is the Taylor diagram for evaluating the GEOS-Chem simulations of surface NO_2 concentrations from 2020 Default, 2020 NOx and 2020 Adjoint using the in-situ measurements.

391   The simulation 2020 Adjoint (inverted triangle in Fig. 7(a)) has the best performance among these

392   three simulations with the lowest relative bias and lowest normalized centered RMSE. Without

393   updating the NOx emission, 2020 Default features a relative bias of ~37%. After updating the NOx

394   emissions, 2020 NOx reduces the relative bias, normalized centered RMSE and normalized

395   standard deviation from around 37%, 1.38 and 1.80 to around 10%, 1.20 and 1.51 compared with

396   2020 Default, but the correlation coefficient also decreases. By using 4D-Var method, 2020

397   Adjoint further reduces the relative bias, normalized centered RMSE and normalized standard

398   deviation and increases the correlation coefficient compared with 2020 NOx. We also validated

399   the VOC emissions by comparing the simulated HCHO VCD with TROPOMI measurements

400   (Appendix D).

401

402
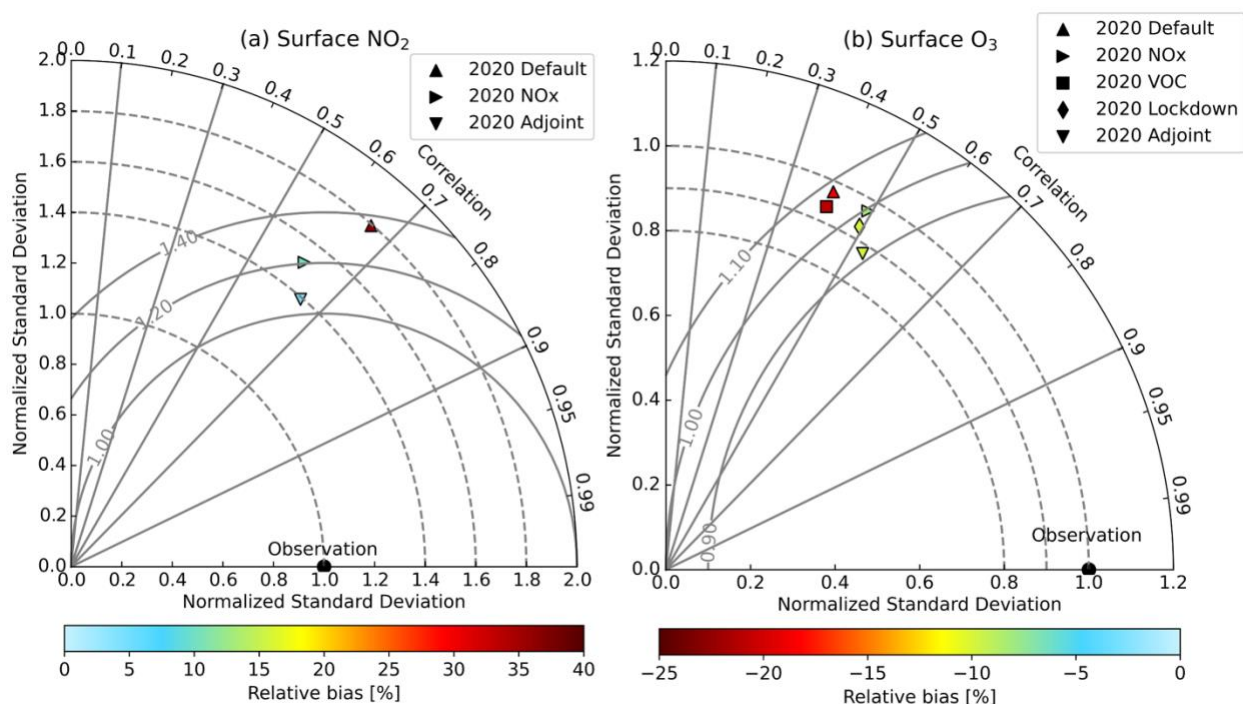
403   **Figure 7.** Taylor diagram for evaluating the GEOS-Chem simulations of (a) surface NO_2 and (b)

404   surface O_3 during lockdown period (2020 Feb.-Mar.) using ground observations for different

405   simulation experiments listed in Table 1. The evaluation of surface O_3 only includes the areas

406   where the NOx emissions optimized by 4D-Var reduced by more than 10%.

407

408

409   **3.3 Evaluation of surface O_3 simulations**

18

410   We evaluated the GEOS-Chem simulations of MDA8 surface O_3 from different simulation

411   experiments listed in Table 1 using ground measurements. Fig. 7(b) is the Taylor diagram for

412   comparing the surface O_3 concentrations during 2020 Feb.-Mar. from ground measurements and

413   GEOS-Chem simulations. We focused on areas with significant NOx emissions reduction to better

414   assess the role of updated NOx emissions in improving surface O_3 simulations. The ground sites

415   where the NOx emissions from 4D-Var decline by less than 10% are excluded. The correlation

416   coefficient between the simulation Baseline (2019) and ground observations is ~0.53 and the

417   relative bias is around -25%. By applying 2020 meteorological fields and scaling the VOC

418   emissions, the correlation coefficients decreased to ~0.40 for model simulations 2020 Default and

419   2020 VOC, with little reduction in the relative bias. By updating the NOx emissions, the relative

420   bias reduced to around -10% while the correlation coefficients remain at ~0.50 for model

421   simulations 2020 NOx, 2020 Lockdown and 2020 Adjoint. This indicates the NOx emission

422   updates significantly improve the surface O_3 simulations. Comparing the simulations 2020 Default

423   and 2020 VOC, or 2020 NOx and 2020 Lockdown, the results show that scaling VOC emissions

424   does not improve the surface O_3 simulations significantly over the continental China, but over

425   South China, VOC emissions update reduces the relative bias by 3%. Among all simulations, 2020

426   Adjoint exhibits the best performance with the lowest normalized centered RMSE, largest

427   correlation coefficient and a low relative bias of ~10%. This result further confirms the superiority

428   of the 4D-Var with respect to the mass balance method for optimizing NOx emissions. Therefore,

429   we used the 2020 Adjoint to evaluate the impacts of NOx emission on surface O_3 in the following

430   analysis.

431   Fig. 8 compares the modeled surface O_3 in Feb.-Mar. of 2019 (Fig. 8(a)) and 2020 (Fig.

432   8(b)) and the relative difference (Fig. 8(c)) computed from Equation (6) with the in-situ

433   measurements (Fig. 8(d-f)). The ground observations show that the highest level of surface O_3

434   pollution occurs in North China and southwest of China. The average MDA8 O_3 in two months

435   can reach up to ~110 $\mu g\ m^{-3}$ at STP (~51.4 ppbv), which is higher than the China National Ambient

436   Air Quality Standard daily maximum 8-hour Grade I standard of 100 $\mu g\ m^{-3}$. GEOS-Chem model

437   underestimates the surface O_3 over North China for both years compared with ground observations,

438   which could be a result of the underestimation of biogenic VOC emissions (Appendix D). The

439   underestimation of the simulated O_3 over North China will not significantly affect our study

440   purpose since this study focuses on revealing the impacts of emissions and meteorology change

441   on the surface O_3 change by each region. The bias is predominantly systematic and will be

442   substantially cancelled when we compute the relative difference of the surface O_3. The model

443   captures the magnitude and spatial distribution of surface O_3 and the increasing trend in South

444   China well. In South China, the measured surface O_3 in 2020 Feb.-Mar. increases by 30-50%,

445   while over North China, it increases generally by less than 20% even decreases in some regions.

446   The relative differences of simulated surface O_3 between two years is comparable to the ground

447   observations over South China (green box in Fig. 8(c, f)). In Sichuan Basin, the trend of the surface

448   O_3 change from the model is opposite to the measurements, which is probably caused by the

449   inaccurate simulation of the meteorological effects (See Section 4.1) due to the complex terrain

450   features in this region. The localized improvement of the model simulation is further needed for

451   the regional study. Over North China (pink box in Fig. 8(c, f)), the average relative difference

452   between two years from the model and observation are 4.27% and -3.01%, respectively, both of

453   which are much smaller than their counterparts in South China. While the relative difference from

454   model simulations has different signs as compared to that of observations on average, both the

455   change of O_3 is indeed small and the model is able to capture the part of O_3 decrease in the

456   southwest part of the North China domain (Fig. 8(c)). We note that some previous studies showed

457   large increase of O_3 in North China, but such increase is in comparison with the O_3 in the month

458   right before the lockdown (not the same time in 2019; (Shi & Brasseur, 2020; Y. M. Liu et al.,

459   2021).

460
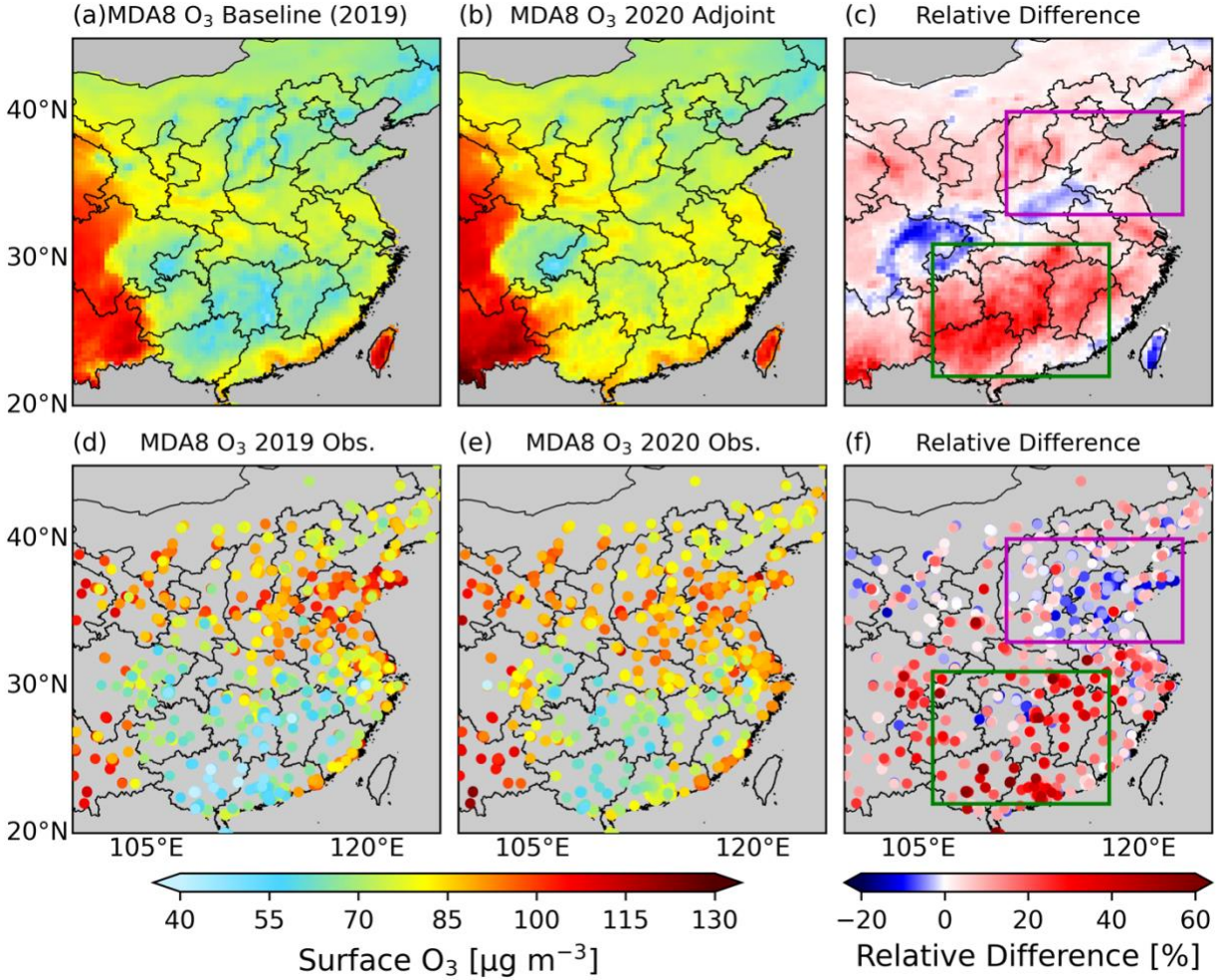
Figure 8. Comparison of MDA8 surface O_3 in 2019 and 2020 Feb.-Mar. and the relative difference between two years from GEOS-Chem model (a-c) versus ground observations (d-f). GEOS-Chem mean MDA8 O_3 at 9 m above the surface under standard temperature and pressure (STP; 273.15 K, 101.325 kPa) from (a) Baseline (2019) and (b) 2020 Adjoint simulation (Table 1) together with (c) their relative difference. Ground observed mean MDA8 surface O3 under STP in (d) 2019 Feb.-Mar.; (e) 2020 Feb.-Mar. and (f) their relative difference. The pink and green boxes in (c) and (f) define the North China and South China domain.

4. Mechanism of aggravated surface O_3 pollution

4.1 Relative contribution from declining emissions and meteorological variations

473   From equations (2)-(5) we can analyze the mechanism of surface O_3 increase in China

474   during the COVID-19 pandemic (Fig. 9). NOx emission reduction as a result of COVID-19

475   lockdown leads to a ~8% increase in the mean MDA8 surface O_3 over North China (pink boxes in

476   Fig. 9) between 2019 and 2020 Feb.-Mar. (Fig. 9(a)), while the VOC emission decline causes ~3%

477   of O_3 decrease (Fig. 9(b)). The average contribution of the meteorological variations to the surface

478   O_3 change is less than 1% in North China (Fig. 9(d)). However, in South China, the inter-annual

479   meteorological variations dominate the surface O_3 increases, causing a ~30% increase (Fig. 9(d)),

480   while the NOx and VOC emission reduction has little impacts. The overall magnitude of emissions

481   contribution to the surface O_3 change over North China is ~5%, similar to that of the

482   meteorological effects, but meteorological variations lead to both O_3 increases and decreases in

483   different regions. Over South China, the meteorological effect is much larger than the net effects

484   of declining emissions. Overall, the impact of inter-annual meteorological variations between 2019

485   and 2020 is almost 30 times larger than the overall emissions impacts on the aggregated surface

486   O_3 pollution in China. Our results are consistent with the conclusion from Zhao et al. (2020) that

487   meteorological variation has larger impacts than emissions reduction on surface O_3 in the southern

488   city of Guangzhou, but in Beijing, emission reduction has a larger impact during 23-29 January.

489   Liu et al. (2020b) reported that the surface O_3 increase in the major cites of the Yangtze River

490   Delta region were driven by both emission reduction and meteorological variations to a similar

491   degree from pre-lockdown period (Jan. 1-22, 2020) to lockdown period (Jan. 23-Feb. 29, 2020).

492   However, Zhao et al. (2020) and Liu et al. (2020b) only focused on the lockdown period of one

493   week in reference to the time period right before the lockdown instead of the same period in

494   previous years, which cannot exclude the effects of seasonal variation of meteorology and did not

495   provide a comprehensive analysis over the whole lockdown period. Moreover, Liu et al. (2020b)

496   only analyzed four representative cities instead of showing the analysis at a national scale. Further,

497   Zhao et al. (2020) did not update the anthropogenic emissions during the lockdown period, which

498   brings significant uncertainties to their analysis. Previous studies found that TROPOMI NO_2

499   product has a negative bias of -7% to -20% (Verhoelst et al., 2021; Judd et al., 2020; Li et al.,

500   2021). The sensitivity simulations indicate this low bias does not significantly affect the model

501   evaluation and our main conclusions (figures not shown).

502

503
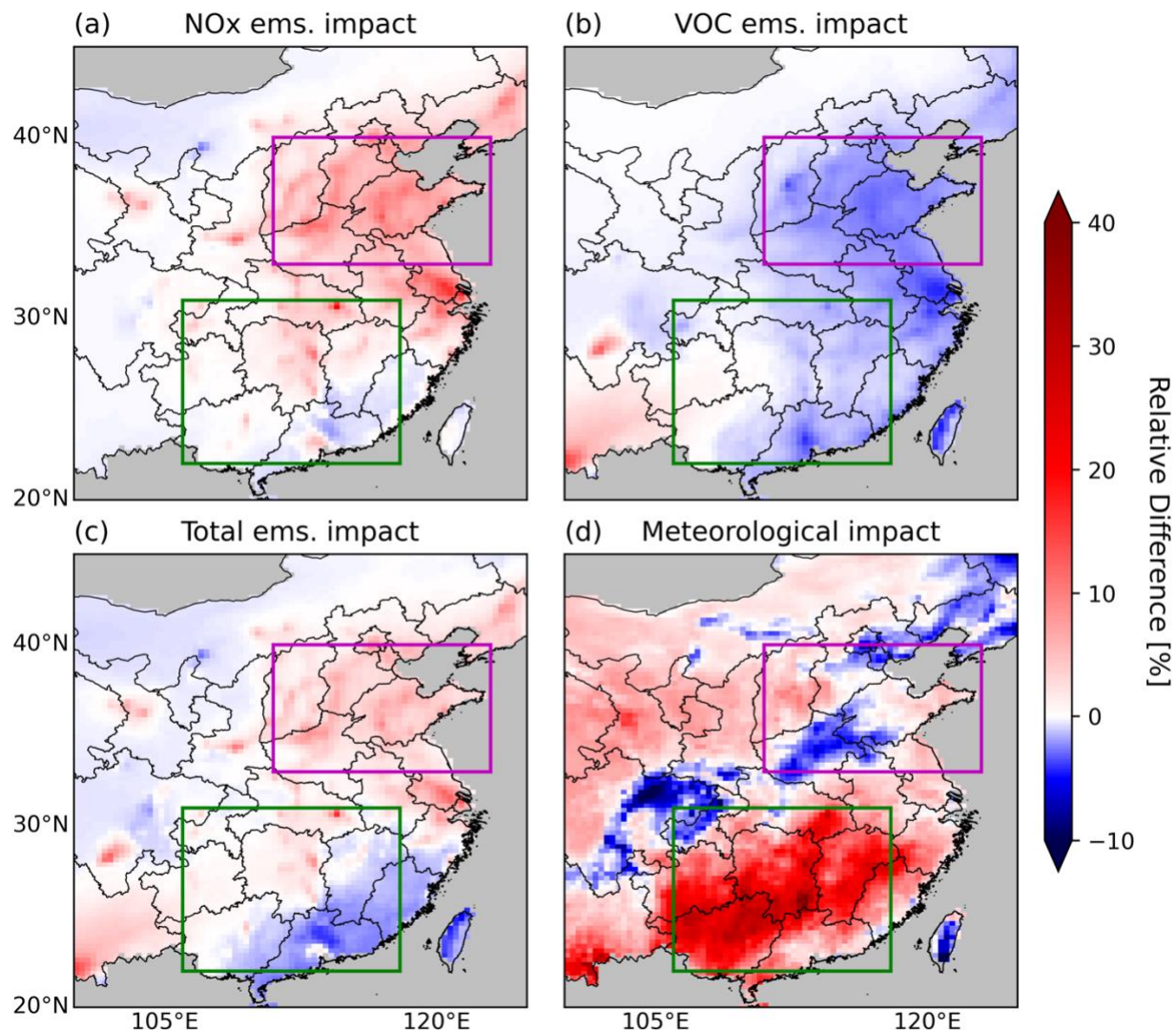
Figure 9. Relative difference in simulated surface O_3 caused by (a) NOx emission reduction, (b) VOC emission reduction, (c) overall emission reduction and (d) meteorological variations due to COVID-19 lockdown. The pink and green boxes in each panel define the North China and South China domain.

4.2 Critical meteorological variables causing aggravated surface O_3 pollution in South China

To identify the critical meteorological variables that lead to the aggravated surface O_3 pollution in South China, we investigated the correlations between the surface O_3 concentrations and 2-m air temperature, downward visible direct flux at surface, cloud fraction, relative humidity, and wind speed. The positive correlation between the surface O_3 and temperature is widely

516   observed and reported in the literature (Pusede et al., 2015). Higher temperature leads to higher

517   concentrations of surface O_3 because it improves the O_3 production rate by affecting the organic

518   reactivity, production of HOx radicals, formation and decomposition of peroxy nitrates and alkyl

519   nitrates (Pusede et al., 2015). We calculated the daily difference in Feb.-Mar. between 2020 and

520   2019 (excluding Feb. 29, 2020) for the daily mean of MDA8 O_3 from ground measurements and

521   2-meter air temperature, downward visible direct flux at surface and cloud fraction from GEOS-

522   FP data used in our GEOS-Chem simulations for the South China (106°E - 118°E, 22°N - 31°N,

523   green box in Fig. 10(a-c)) and North China (111°E - 123°E, 33°N - 40°N, pink box in Fig. 10(a-

524   c)). Fig. 10 displays the difference of 2-month mean 2-meter air temperature (Fig. 10(a)),

525   downward visible direct flux at surface (Fig. 10(b)) and cloud fraction (Fig. 10(c)) in Feb.-Mar.

526   between 2020 and 2019 and the scatter plot between the daily difference of measured surface O_3

527   concentration and 2-meter air temperature (Fig. 10(d)), downward visible direct flux at surface

528   (Fig. 10(e)) and cloud fraction (Fig. 10(f)) over both South China (green dots in Fig. 10(d-f)) and

529   North China (pink dots in Fig. 10(d-f)). We found the 2-meter air temperature increased by ~2.3°C

530   in South China, and the daily difference of surface O_3 concentration and 2-meter air temperature

531   are well correlated with a positive correlation coefficient of 0.612. Therefore, the temperature

532   increase contributed to the significant aggravated surface O_3 pollution in South China. The

533   enhanced solar radiation at surface could also promote the production of O_3 via photochemical

534   reactions. The correlation coefficient between the daily difference of surface O_3 concentration and

535   downward visible direct flux at surface is as high as 0.740 in South China (Fig. 10(e)). The reason

536   for the increase of temperature and solar radiation at surface is the lower cloud fraction. Via

537   analyzing the GEOS-FP data, we found the cloud fraction decreases by ~5% (Fig. 10(c)), and the

538   downward visible direct flux at surface increased by 5 W m^{-2} (Fig. 10(b)) over South China. The

539   lower cloud fraction increases the downward solar radiation at the surface during the lockdown

540   period, leading to higher surface air temperature. The change of cloud fraction is negatively

541   correlated with the change of surface O_3 in South China with the correlation coefficient of -0.619

542   (Fig. 10(f)).

543   In North China, 2-meter air temperature also increased by 1.8°C, but the measured surface

544   MDA8 O_3 decreased by 3% (Fig. 8(f)). Fig. 10(d) shows the daily difference of MDA8 O_3 and 2-

545   meter air temperature over North China also has a high correlation coefficient of 0.731. However,

546   the intercept of the linear regression line is negative, so that the surface O_3 could decrease even

547 though the temperature increases. This negative intercept is caused by the net effects of factors
548 other than temperature, including chemistry, emissions, and other meteorological factors. It is a
549 challenge to quantify the contributions of each individual factors, because these factors are
550 thermodynamically or dynamically related. The predicted average change of surface MDA8 O_3 in
551 South China and North China are marked by the green and pink open squares respectively in Fig.
552 10(d) based on the linear regression. Because of the different intercepts, the predicted MDA8 O_3
553 in South China increases by ~9.0 µg m^{-3}, while it decreases by 2.2 µg m^{-3} in North China, although
554 the average temperature increased in both South and North China. On the contrary to South China,
555 the change of solar radiation at surface and cloud fraction are poorly correlated with the change of
556 surface O_3 concentrations in North China (Fig. 10(e, f)), mainly due to a more important role of
557 emission change in regulating the surface O_3 in North China.

558

559
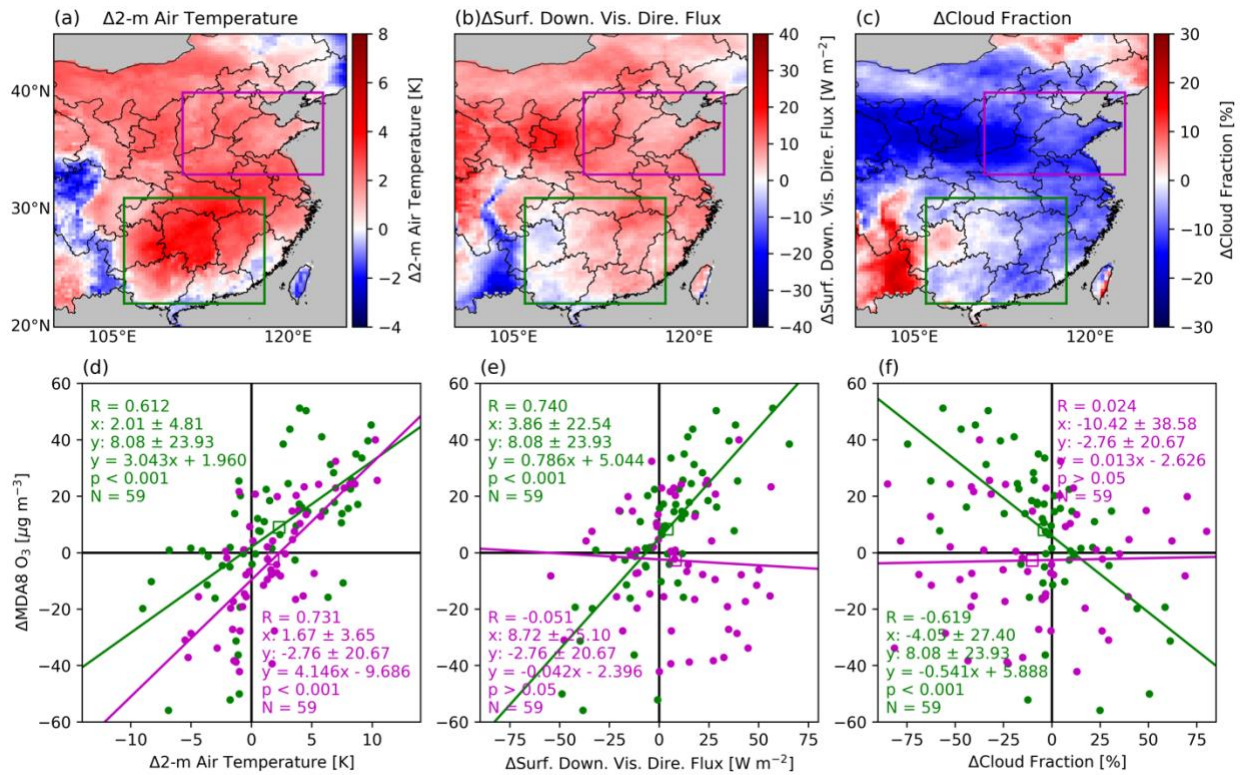
560 **Figure 10.** The changes of (a) 2-meter air temperature, (b) downward visible direct flux at surface
561 and (c) cloud fraction from 2019 Feb.-Mar. to 2020 Feb.-Mar and the scatter plots between the
562 daily difference of surface O_3 measurements and (d) 2-meter air temperature, (e) downward visible
563 direct flux at surface and (f) cloud fraction in Feb.-Mar. between 2020 and 2019 over South China
564 (green dots) and North China (pink dots). The green and pink open squares in (d-f) mark the

565   predicted average change of surface MDA8 O_3 in South China and North China, respectively,

566   based on the linear regression against the change of meteorological variables.

567

568   The impacts of relative humidity and wind speed on the surface O_3 change are also

569   investigated (Fig. 11). The relative humidity increased by ~5.1% in North China and decreased by

570   ~3.0% in South China on average. The strong correlation (R = -0.675) between the change of

571   relative humidity and surface O_3 in South China indicates the decrease of relative humidity also

572   contributes to the increase of surface O_3 pollution in South China, but the correlation between them

573   in North China is very low. The wind speed also changed oppositely in South China and North

574   China, but we cannot identify any significant impact of wind speed on the surface O_3 pollution

575   since the correlation coefficients are low in both South China and North China. In summary, the

576   significant increase of surface O_3 pollution during the lockdown period in South China could be

577   primarily attributed to the higher temperature, enhanced solar radiation at surface and declined

578   relative humidity.
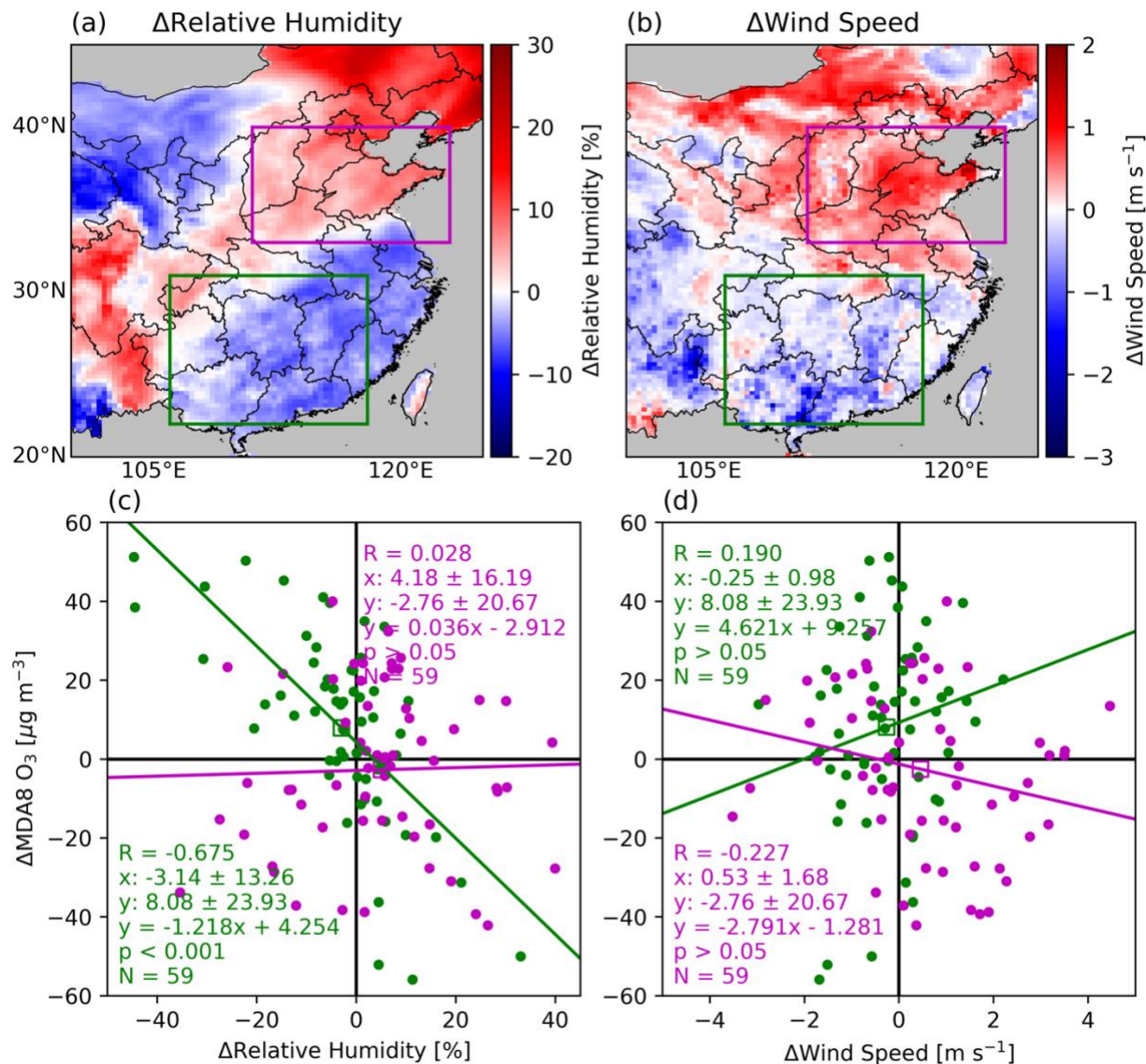
Figure 11. Same as Fig. 10 but for (a, c) relative humidity and (b, d) wind speed.

5. Summary

A significant reduction in primary air pollutants has been identified by surface and satellite observations during the COVID-19 pandemic in China (Bauwens et al., 2020; Miyazaki et al., 2020), which is in contrast to the increase of surface O_3. In this study, we analyzed the reasons for the enhanced surface O_3 pollution from two perspectives: anthropogenic emissions reduction and inter-annual meteorological variations. We constrain the NOx emissions based on the TROPOMI NO_2 product using both the mass balance and 4D-Var methods. The VOC emissions were also updated based on the TROPOMI HCHO product via the mass balance approach. We analyzed the

27

590   contributions from emissions reduction and meteorological variations to surface O_3 increases
591   through a series of sensitivity simulations using the GEOS-Chem model.

592   The updated NOx emissions from the 4D-Var and mass balance approaches share a similar
593   spatial pattern. However, the NOx emissions from 4D-Var are lower than those from the mass
594   balance method over North China by ~10% but larger over central China by ~40%. The evaluation
595   of the simulations with the updated emissions against the TROPOMI NO_2, in-situ measurements
596   of surface NO_2 and O_3 indicate that the NOx emissions from the 4D-Var inversion leads to better
597   model performance than that from the mass balance approach.

598   The anthropogenic NOx emission decreased by ~30% over East China during 2020 Feb.-
599   Mar. compared to the same period in 2019. Over North China, NOx emission reduction leads to a
600   ~8% increase in the mean MDA8 surface O_3, while the VOC emissions decline causes O_3 to
601   decrease by ~3%. The average contribution of meteorological variations to the surface O_3 change
602   is less than 1% in North China. However, in South China, the inter-annual meteorological variation
603   dominates the surface O_3 increase, causing a ~30% increase, while the NOx and VOC emission
604   reduction has nearly no impacts on O_3. Overall, the impact of inter-annual meteorological
605   variations between 2019 and 2020 is almost 30 times larger than the impact of emissions on the
606   enhanced surface O_3 pollution in China.

607   The significant increase of surface O_3 in South China could be attributed to the higher
608   temperature, enhanced solar radiation at surface and declined relative humidity during the
609   lockdown period. The lower cloud fraction increases the downward solar radiation at the surface
610   during the lockdown period, leading to higher surface air temperature. We cannot identify any
611   significant impact of wind speed on the surface O_3 pollution.

612

613

Appendix A: NOx emission reduction in China from 2010 to 2019

615   The default anthropogenic NOx emission over East Asia in GEOS-Chem is MIX 2010 (Li
616   et al., 2017).To generate the anthropogenic NOx emission in 2019, we calculated the ratio of mean
617   TROPOMI tropospheric NO_2 VCD in Feb.-Mar. 2019 to GEOS-Chem simulated NO_2 VCD with
618   the default MIX 2010 emission as the scaling factor (Fig. A1). The scaling factors in regions where
619   mean TROPOMI tropospheric NO_2 VCD in 2019 Feb.-Mar. less than 0.1 DU are set to 1. From

620   2010 to 2019, the anthropogenic NOx emission has declined significantly as a result of the clean
621   air actions of Chinese government (Zheng et al., 2018).
622

623
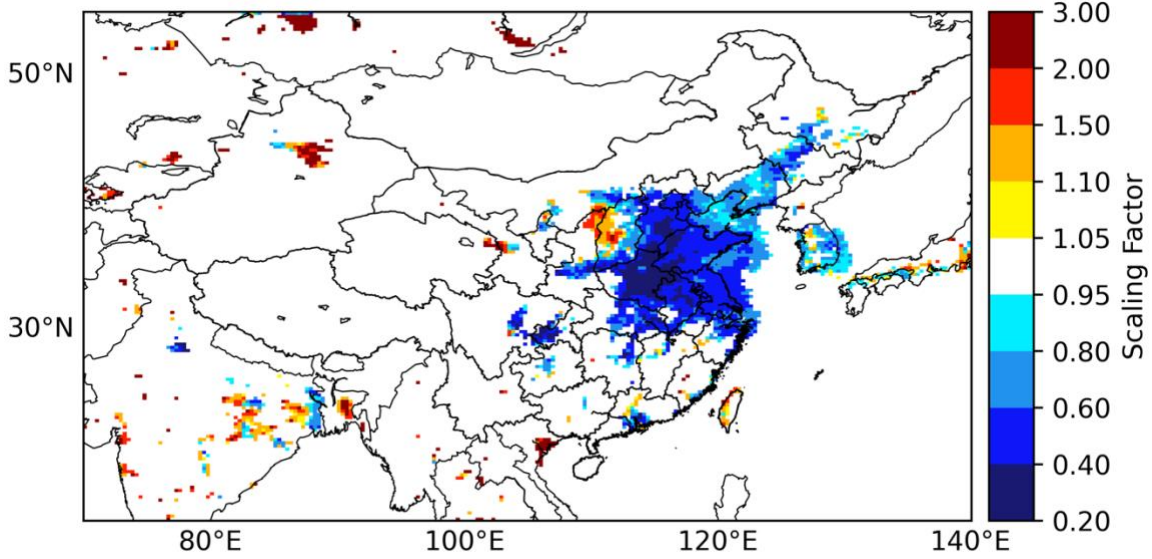
624   **Figure A1.** The scaling factor of anthropogenic NOx emission from year 2010 to 2019.

625

626

627   **Appendix B: Applying the TROPOMI NO$_2$ averaging kernel in the observation**

628   **operator**

629   To optimize the NOx emissions and minimize the cost function (Equation (1)) with the 4D-

630   Var method, GEOS-Chem adjoint needs to compute the derivative of the cost function with respect

631   to the model parameters to be optimized, which is the scaling factors of the anthropogenic NOx

632   emissions in this study. An essential step is to calculate the adjoint forcing $\boldsymbol{F}$, which is the

633   derivative of the cost function with respect to the modeled NO$_2$ concentration shown as Equation

634   (B1).

$$\boldsymbol{F} = \frac{\partial J}{\partial \boldsymbol{c}} = \boldsymbol{S}_{\mathrm{obs}}^{-1}[H(\boldsymbol{c}) - \boldsymbol{s}]\frac{\partial H(\boldsymbol{c})}{\partial \boldsymbol{c}} \tag{B1}$$

636   For each single TROPOMI NO$_2$ observation, the adjoint forcing component f and cost function

637   component j are computed as Equation (B2) and Equation (B3).

$$f = \frac{M_{\mathrm{gc}}v_{\mathrm{gc}} - M_{\mathrm{obs}}v_{\mathrm{obs}}}{e_{\mathrm{obs}}M_{\mathrm{obs}}}M_{\mathrm{gc}} \tag{B2}$$

$$j = \frac{0.5f\left(M_{gc}v_{gc} - M_{obs}v_{obs}\right)}{M_{gc}} \tag{B3}$$

Here M_{gc} is GEOS-Chem air mass factor applying the GEOS-Chem NO_2 vertical profiles and TROPOMI NO_2 averaging kernel. M_{obs} is TROPOMI air mass factor. v_{gc} and v_{obs} are the tropospheric NO_2 VCD from GEOS-Chem model and TROPOMI observation, respectively. The product of air mass factor and NO_2 VCD is NO_2 slant column density. e_{obs} is the standard error of TROPOMI tropospheric NO_2 VCD.

We calculated the GEOS-Chem air mass factor M_{gc} as Equation (B4) following Qu et al. (2019).

$$M_{gc} = \frac{\sum_{i \in trop.} c_i^{gc} \Delta p_i^{gc} w_i^{gc}}{\sum_{i \in trop.} c_i^{gc} \Delta p_i^{gc}} \tag{B4}$$

Here c_i^{gc} is GEOS-Chem NO_2 mixing ratio at vertical layer i, Δp_i^{gc} is the pressure difference between the GEOS-Chem vertical layer i and $i+1$. w_i^{gc} is the scattering weight at the GEOS-Chem vertical layer i, which is calculated by the linear interpolation of the scattering weights at the vertical coordinate of the model TM5 used for TROPOMI NO_2 retrieval. The scattering weight at the TM5 vertical layer l (w_l^{TM5}) is computed as the product of TROPOMI air mass factor and the TROPOMI averaging kernel at the TM5 vertical layer l (A_l^{TM5}) using Equation (B5-B6) (Eskes and Boersma, 2003; Palmer et al., 2001).

$$w_l^{TM5} = \frac{M_{obs}A_l^{TM5}}{M_{geo}} \tag{B5}$$

$$M_{geo} = \sec\theta_0 + \sec\theta \tag{B6}$$

where M_{geo} is geometric air mass factor, θ_0 and θ are solar zenith angle and viewing zenith angle, respectively.

Appendix C: Validation of the TROPOMI NO_2 observation operator

We validated the observation operator by comparing the sensitivity of the cost function with respect to the emission scaling factor from GEOS-Chem adjoint and a finite difference estimation as shown in Equation (C1). We shut down the transport and exclude a priori term from the cost function for the validation, so that the gradient of cost function component in each grid

665 cell to the local emission scaling factor equals to the gradient of total cost function to the emission
666 scaling factor in the same grid cell.

$$\frac{\partial J(\ln \sigma)}{\partial \ln \sigma} \approx \frac{J(\ln(\sigma + 0.05)) - J(\ln(\sigma - 0.05))}{\ln(\sigma + 0.05) - \ln(\sigma - 0.05)} \tag{C1}$$

668 Fig. C1 compared the cost function sensitivities calculated from GEOS-Chem adjoint and
669 the finite difference method for the nested grids with the spatial resolution of 0.25°×0.3125°. The
670 spatial pattern and magnitude of the cost function sensitivities from the two methods match with
671 each other with a correlation coefficient of 0.97. The statistics show that the agreement of the
672 adjoint sensitivities and finite difference sensitivities in this study is comparable to that in Wang
673 et al. (2020a) although we constrain the NOx emission at a much finer resolution of 0.25°×0.3125°
674 than in their study (2°×2.5°).

675
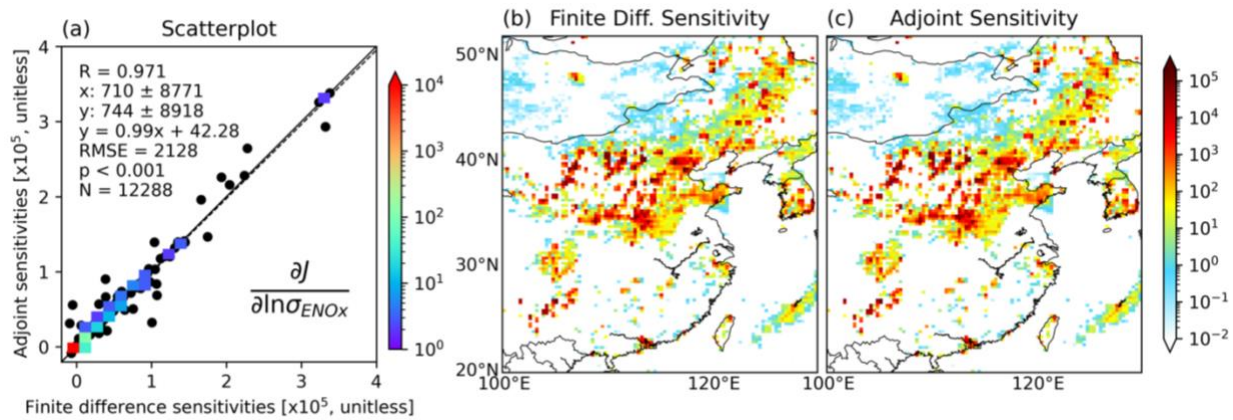
677 **Figure C1.** Comparison of adjoint sensitivities and finite difference sensitivities. (a) Scatter plot
678 of the adjoint sensitivity of the cost function with respect to the logarithm of NOx emission scaling
679 factor versus the finite difference sensitivities. The color scheme for panel (a) encodes the number
680 of samples (the legend on the right of panel (a)). (b) Map of finite difference sensitivity. (c) Map
681 of adjoint sensitivity.

682

683 **Appendix D: Validation of HCHO simulations**

684 It is not practical to validate the VOC emissions species by species in this study. We
685 compare the GEOS-Chem simulation of HCHO with TROPOMI data for a rough validation of the
686 VOC emissions. Overall, the GEOS-Chem simulations Baseline (2019) and 2020 Adjoint agree
687 well with TROPOMI HCHO in Feb.-Mar. of 2019 and 2020, respectively (Fig. D1). The

688   correlation coefficients for the two comparisons are 0.878 and 0.874, and the MBE are -0.036 DU

689   and -0.042 DU, respectively. This good agreement also supports our assumption of ignoring the

690   change of VOC emissions from 2010 to 2019, since the anthropogenic VOC emission used for

691   Baseline (2019) is equivalent to MIX 2010. However, Fig. D1 shows GEOS-Chem tends to

692   overestimate the HCHO VCD over urban regions and underestimate it over rural regions, which

693   indicates the partition of total emissions may overestimate the anthropogenic emissions and

694   underestimate the biogenic emissions, at least for HCHO. A more comprehensive evaluation for

695   various species and emission sectors would be helpful for further improvement of the VOC

696   emissions used in the model.

697

698
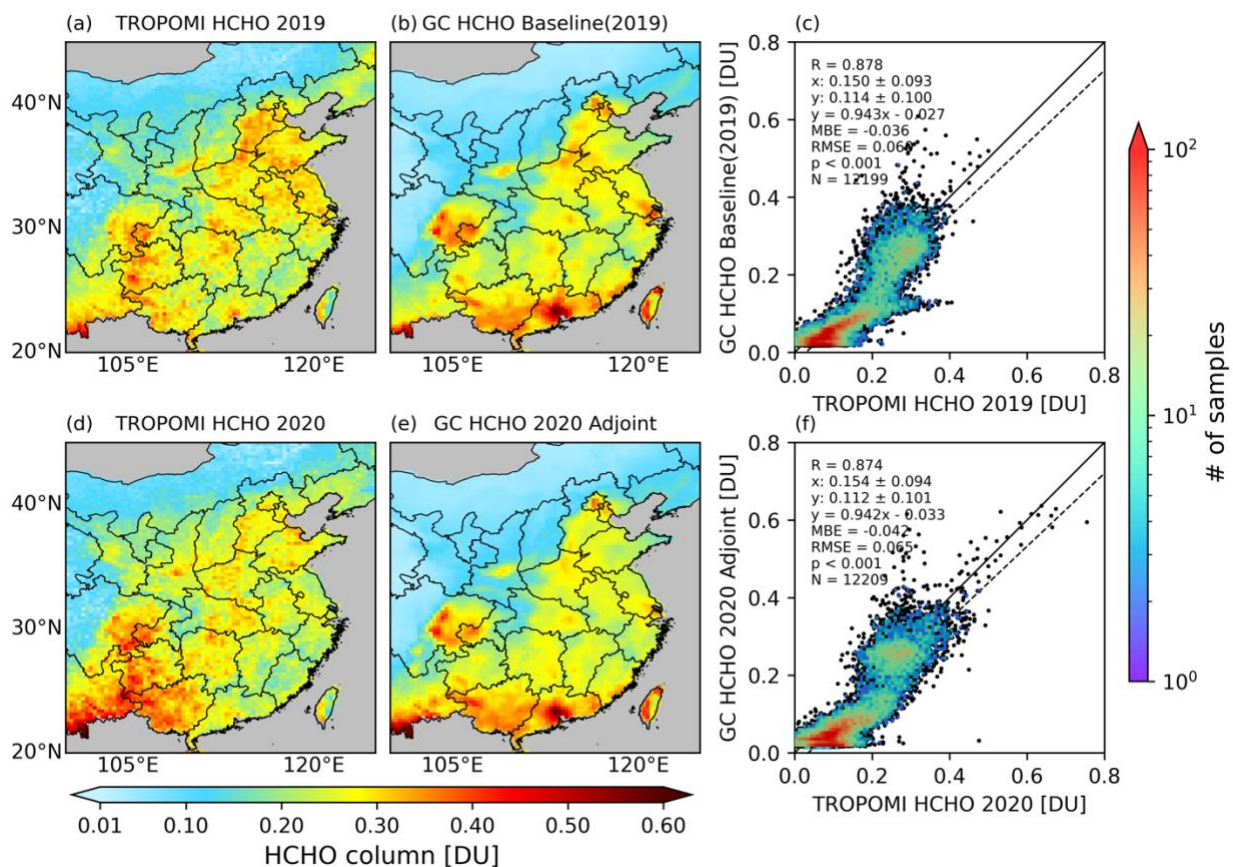
699   **Figure D1.** Comparison of tropospheric HCHO VCD from TROPOMI and GEOS-Chem. (a):

700   TROPOMI HCHO in 2019 Feb.-Mar. (b): GEOS-Chem HCHO from Baseline (2019). (c): Scatter

701   plot between (a) and (b). (d): TROPOMI HCHO in 2020 Feb. -Mar. (e): GEOS-Chem HCHO from

702   2020 Adjoint. (f): Scatter plot between (d) and (e). The emissions and meteorology configurations

703   for GEOS-Chem simulations Baseline (2019) and 2020 Adjoint are listed in Table 1.

Data availability

The TROPOMI NO_2 and HCHO product are available at the NASA Goddard Earth Sciences Data and Information Services Center (https://daac.gsfc.nasa.gov). The ground O_3 and NO_2 measurements are available at the China National Environmental Monitoring Center (http://www.cnemc.cn/en/).

Author contribution

ZL and JW designed the research, and ZL conducted the research. YW, DKH and XC contributed to the research design. ZL and JW wrote the manuscript, and XC and DKH contributed to the writing. YW and TS developed the codes for comparing the tropospheric NO_2 VCD from model and TROPOMI data. KS developed the codes for oversampling.

Competing interests

The authors declare that they have no conflict of interest.

Acknowledgements

References

Atkinson, R.: Atmospheric chemistry of VOCs and NOx, Atmospheric Environment, 34, 2063-2101, 10.1016/s1352-2310(99)00460-4, 2000.

Bauwens, M., Compernolle, S., Stavrakou, T., Muller, J. F., van Gent, J., Eskes, H., Levelt, P. F., van der A, R., Veefkind, J. P., Vlietinck, J., Yu, H., and Zehner, C.: Impact of Coronavirus

Outbreak on NO2 Pollution Assessed Using TROPOMI and OMI Observations, Geophys Res Lett, 47, 10.1029/2020GL087978, 2020.

Bey, I., Jacob, D. J., Yantosca, R. M., Logan, J. A., Field, B. D., Fiore, A. M., Li, Q., Liu, H. Y., Mickley, L. J., and Schultz, M. G.: Global modeling of tropospheric chemistry with assimilated meteorology: Model description and evaluation, Journal of Geophysical Research: Atmospheres, 106, 23073-23095, 10.1029/2001jd000807, 2001.

Bi, Z., Ye, Z., He, C., and Li, Y.: Analysis of the meteorological factors affecting the short-term increase in O3 concentrations in nine global cities during COVID-19, Atmospheric Pollution Research, 13, 101523, https://doi.org/10.1016/j.apr.2022.101523, 2022.

Chen, D., Wang, Y., McElroy, M. B., He, K., Yantosca, R. M., and Le Sager, P.: Regional CO pollution and export in China simulated by the high-resolution nested-grid GEOS-Chem model, Atmospheric Chemistry and Physics, 9, 3825-3839, 10.5194/acp-9-3825-2009, 2009.

Cooper, M., Martin, R. V., Padmanabhan, A., and Henze, D. K.: Comparing mass balance and adjoint methods for inverse modeling of nitrogen dioxide columns for global nitrogen oxide emissions, Journal of Geophysical Research: Atmospheres, 122, 4718-4734, 10.1002/2016jd025985, 2017.

De Smedt, I., Theys, N., Yu, H., Danckaert, T., Lerot, C., Compernolle, S., Van Roozendael, M., Richter, A., Hilboll, A., Peters, E., Pedergnana, M., Loyola, D., Beirle, S., Wagner, T., Eskes, H., van Geffen, J., Boersma, K. F., and Veefkind, P.: Algorithm theoretical baseline for formaldehyde retrievals from S5P TROPOMI and from the QA4ECV project, Atmospheric Measurement Techniques, 11, 2395-2426, 10.5194/amt-11-2395-2018, 2018.

Eskes, H. J. and Boersma, K. F.: Averaging kernels for DOAS total-column satellite retrievals, Atmospheric Chemistry and Physics, 3, 1285-1291, 10.5194/acp-3-1285-2003, 2003.

Ghahremanloo, M., Lops, Y., Choi, Y., and Mousavinezhad, S.: Impact of the COVID-19 outbreak on air pollution levels in East Asia, Science of the Total Environment, 754, 10.1016/j.scitotenv.2020.142226, 2021.

Gong, C., Lei, Y., Ma, Y., Yue, X., and Liao, H.: Ozone–vegetation feedback through dry deposition and isoprene emissions in a global chemistry–carbon–climate model, Atmos. Chem. Phys., 20, 3841-3857, 10.5194/acp-20-3841-2020, 2020.

Guenther, A. B., Jiang, X., Heald, C. L., Sakulyanontvittaya, T., Duhl, T., Emmons, L. K., and Wang, X.: The Model of Emissions of Gases and Aerosols from Nature version 2.1 (MEGAN2.1):

765 an extended and updated framework for modeling biogenic emissions, Geoscientific Model
766 Development, 5, 1471-1492, 10.5194/gmd-5-1471-2012, 2012.

767 Guo, J., Zhang, X. S., Gao, Y., Wang, Z. W., Zhang, M. G., Xue, W. B., Herrmann, H., Brasseur,
768 G. P., Wang, T., and Wang, Z.: Evolution of Ozone Pollution in China: What Track Will It Follow?,
769 Environmental Science & Technology, 57, 109-117, 10.1021/acs.est.2c08205, 2023.

770 Henze, D. K., Hakami, A., and Seinfeld, J. H.: Development of the adjoint of GEOS-Chem,
771 Atmospheric Chemistry and Physics, 7, 2413-2433, 10.5194/acp-7-2413-2007, 2007.

772 Henze, D. K., Seinfeld, J. H., and Shindell, D. T.: Inverse modeling and mapping US air quality
773 influences of inorganic PM2.5 precursor emissions using the adjoint of GEOS-Chem, Atmospheric
774 Chemistry and Physics, 9, 5877-5903, 10.5194/acp-9-5877-2009, 2009.

775 Hoesly, R. M., Smith, S. J., Feng, L., Klimont, Z., Janssens-Maenhout, G., Pitkanen, T., Seibert,
776 J. J., Vu, L., Andres, R. J., Bolt, R. M., Bond, T. C., Dawidowski, L., Kholod, N., Kurokawa, J.-
777 i., Li, M., Liu, L., Lu, Z., Moura, M. C. P., O'Rourke, P. R., and Zhang, Q.: Historical (1750–2014)
778 anthropogenic emissions of reactive gases and aerosols from the Community Emissions Data
779 System (CEDS), Geoscientific Model Development, 11, 369-408, 10.5194/gmd-11-369-2018,
780 2018.

781 Huang, X., Ding, A., Gao, J., Zheng, B., Zhou, D., Qi, X., Tang, R., Wang, J., Ren, C., Nie, W.,
782 Chi, X., Xu, Z., Chen, L., Li, Y., Che, F., Pang, N., Wang, H., Tong, D., Qin, W., Cheng, W., Liu,
783 W., Fu, Q., Liu, B., Chai, F., Davis, S. J., Zhang, Q., and He, K.: Enhanced secondary pollution
784 offset reduction of primary emissions during COVID-19 lockdown in China, National Science
785 Review, 8, 10.1093/nsr/nwaa137, 2020.

786 Hudman, R. C., Moore, N. E., Mebust, A. K., Martin, R. V., Russell, A. R., Valin, L. C., and
787 Cohen, R. C.: Steps towards a mechanistic model of global soil nitric oxide emissions:
788 implementation and space based-constraints, Atmospheric Chemistry and Physics, 12, 7779-7795,
789 10.5194/acp-12-7779-2012, 2012.

790 Janssens-Maenhout, G., Crippa, M., Guizzardi, D., Dentener, F., Muntean, M., Pouliot, G.,
791 Keating, T., Zhang, Q., Kurokawa, J., Wankmuller, R., van der Gon, H. D., Kuenen, J. J. P.,
792 Klimont, Z., Frost, G., Darras, S., Koffi, B., and Li, M.: HTAP_v2.2: a mosaic of regional and
793 global emission grid maps for 2008 and 2010 to study hemispheric transport of air pollution,
794 Atmospheric Chemistry and Physics, 15, 11411-11432, 10.5194/acp-15-11411-2015, 2015.

795   Jerrett, M., Burnett, R. T., Pope, C. A., Ito, K., Thurston, G., Krewski, D., Shi, Y. L., Calle, E.,

796   and Thun, M.: Long-Term Ozone Exposure and Mortality, New England Journal of Medicine, 360,

797   1085-1095, 10.1056/NEJMoa0803894, 2009.

798   Judd, L. M., Al-Saadi, J. A., Szykman, J. J., Valin, L. C., Janz, S. J., Kowalewski, M. G., Eskes,

799   H. J., Veefkind, J. P., Cede, A., Mueller, M., Gebetsberger, M., Swap, R., Pierce, R. B., Nowlan,

800   C. R., Abad, G. G., Nehrir, A., and Williams, D.: Evaluating Sentinel-5P TROPOMI tropospheric

801   NO2 column densities with airborne and Pandora spectrometers near New York City and Long

802   Island Sound, Atmospheric Measurement Techniques, 13, 6113-6140, 10.5194/amt-13-6113-2020,

803   2020.

804   Le, T. H., Wang, Y., Liu, L., Yang, J. N., Yung, Y. L., Li, G. H., and Seinfeld, J. H.: Unexpected

805   air pollution with marked emission reductions during the COVID-19 outbreak in China, Science,

806   369, 702-706, 10.1126/science.abb7431, 2020.

807   Leue, C., Wenig, M., Wagner, T., Klimm, O., Platt, U., and Jähne, B.: Quantitative analysis of

808   NOx emissions from Global Ozone Monitoring Experiment satellite image sequences, Journal of

809   Geophysical Research: Atmospheres, 106, 5493-5505, 10.1029/2000jd900572, 2001.

810   Levelt, P. F., Zweers, D. C. S., Aben, I., Bauwens, M., Borsdorff, T., De Smedt, I., Eskes, H. J.,

811   Lerot, C., Loyola, D. G., Romahn, F., Stavrakou, T., Theys, N., Van Roozendael, M., Veefkind, J.

812   P., and Verhoelst, T.: Air quality impacts of COVID-19 lockdown measures detected from space

813   using high spatial resolution observations of multiple trace gases from Sentinel-5P/TROPOMI,

814   Atmospheric Chemistry and Physics, 22, 10319-10351, 10.5194/acp-22-10319-2022, 2022.

815   Li, M., McDonald, B. C., McKeen, S. A., Eskes, H., Levelt, P., Francoeur, C., Harkins, C., He, J.,

816   Barth, M., Henze, D. K., Bela, M. M., Trainer, M., de Gouw, J. A., and Frost, G. J.: Assessment

817   of Updated Fuel-Based Emissions Inventories Over the Contiguous United States Using

818   TROPOMI   NO2   Retrievals,   Journal   of   Geophysical   Research-Atmospheres,   126,

819   10.1029/2021jd035484, 2021.

820   Li, M., Zhang, Q., Kurokawa, J.-i., Woo, J.-H., He, K., Lu, Z., Ohara, T., Song, Y., Streets, D. G.,

821   Carmichael, G. R., Cheng, Y., Hong, C., Huo, H., Jiang, X., Kang, S., Liu, F., Su, H., and Zheng,

822   B.: MIX: a mosaic Asian anthropogenic emission inventory under the international collaboration

823   framework of the MICS-Asia and HTAP, Atmospheric Chemistry and Physics, 17, 935-963,

824   10.5194/acp-17-935-2017, 2017.

825   Liu, F., Page, A., Strode, S. A., Yoshida, Y., Choi, S., Zheng, B., Lamsal, L. N., Li, C., Krotkov,

826   N. A., Eskes, H., van der A, R., Veefkind, P., Levelt, P. F., Hauser, O. P., and Joiner, J.: Abrupt

827   decline in tropospheric nitrogen dioxide over China after the outbreak of COVID-19, Science

828   Advances, 6, 10.1126/sciadv.abc2992, 2020a.

829   Liu, S. C., Trainer, M., Fehsenfeld, F. C., Parrish, D. D., Williams, E. J., Fahey, D. W., Hubler,

830   G., and Murphy, P. C.: Ozone production in the rural troposphere and the implications for regional

831   and global ozone distributions, Journal of Geophysical Research-Atmospheres, 92, 4191-4207,

832   10.1029/JD092iD04p04191, 1987.

833   Liu, T., Wang, X., Hu, J., Wang, Q., An, J., Gong, K., Sun, J., Li, L., Qin, M., Li, J., Tian, J.,

834   Huang, Y., Liao, H., Zhou, M., Hu, Q., Yan, R., Wang, H., and Huang, C.: Driving Forces of

835   Changes in Air Quality during the COVID-19 Lockdown Period in the Yangtze River Delta

836   Region, China, Environmental Science & Technology Letters, 7, 779-786,

837   10.1021/acs.estlett.0c00511, 2020b.

838   Liu, Y. M., Wang, T., Stavrakou, T., Elguindi, N., Doumbia, T., Granier, C., Bouarar, I., Gaubert,

839   B., and Brasseur, G. P.: Diverse response of surface ozone to COVID-19 lockdown in China,

840   Science of the Total Environment, 789, 10.1016/j.scitotenv.2021.147739, 2021.

841   Lu, X., Zhang, L., Chen, Y. F., Zhou, M., Zheng, B., Li, K., Liu, Y. M., Lin, J. T., Fu, T. M., and

842   Zhang, Q.: Exploring 2016-2017 surface ozone pollution over China: source contributions and

843   meteorological influences, Atmospheric Chemistry and Physics, 19, 8339-8361, 10.5194/acp-19-

844   8339-2019, 2019.

845   Mao, J., Paulot, F., Jacob, D. J., Cohen, R. C., Crounse, J. D., Wennberg, P. O., Keller, C. A.,

846   Hudman, R. C., Barkley, M. P., and Horowitz, L. W.: Ozone and organic nitrates over the eastern

847   United States: Sensitivity to isoprene chemistry, Journal of Geophysical Research: Atmospheres,

848   118, 11,256-211,268, 10.1002/jgrd.50817, 2013.

849   Mao, J., Jacob, D. J., Evans, M. J., Olson, J. R., Ren, X., Brune, W. H., Clair, J. M. S., Crounse, J.

850   D., Spencer, K. M., Beaver, M. R., Wennberg, P. O., Cubison, M. J., Jimenez, J. L., Fried, A.,

851   Weibring, P., Walega, J. G., Hall, S. R., Weinheimer, A. J., Cohen, R. C., Chen, G., Crawford, J.

852   H., McNaughton, C., Clarke, A. D., Jaeglé, L., Fisher, J. A., Yantosca, R. M., Le Sager, P., and

853   Carouge, C.: Chemistry of hydrogen oxide radicals (HOx) in the Arctic troposphere in spring,

854   Atmospheric Chemistry and Physics, 10, 5823-5838, 10.5194/acp-10-5823-2010, 2010.

855   Martin, R. V., Jacob, D. J., Chance, K., Kurosu, T. P., Palmer, P. I., and Evans, M. J.: Global

856   inventory of nitrogen oxide emissions constrained by space-based observations of NO2 columns,

857   Journal of Geophysical Research-Atmospheres, 108, 10.1029/2003jd003453, 2003.

858   Miyazaki, K., Bowman, K., Sekiya, T., Jiang, Z., Chen, X., Eskes, H., Ru, M., Zhang, Y., and

859   Shindell, D.: Air Quality Response in China Linked to the 2019 Novel Coronavirus (COVID-19)

860   Lockdown, Geophys Res Lett, 47, 10.1029/2020gl089252, 2020.

861   Murray, L. T., Jacob, D. J., Logan, J. A., Hudman, R. C., and Koshak, W. J.: Optimized regional

862   and interannual variability of lightning in a global chemical transport model constrained by

863   LIS/OTD satellite data, Journal of Geophysical Research: Atmospheres, 117,

864   10.1029/2012jd017934, 2012.

865   Ott, L. E., Pickering, K. E., Stenchikov, G. L., Allen, D. J., DeCaria, A. J., Ridley, B., Lin, R.-F.,

866   Lang, S., and Tao, W.-K.: Production of lightning NOx and its vertical distribution calculated from

867   three-dimensional cloud-scale chemical transport model simulations, Journal of Geophysical

868   Research, 115, 10.1029/2009jd011880, 2010.

869   Palmer, P. I., Jacob, D. J., Chance, K., Martin, R. V., Spurr, R. J. D., Kurosu, T. P., Bey, I.,

870   Yantosca, R., Fiore, A., and Li, Q. B.: Air mass factor formulation for spectroscopic measurements

871   from satellites: Application to formaldehyde retrievals from the Global Ozone Monitoring

872   Experiment, Journal of Geophysical Research-Atmospheres, 106, 14539-14550,

873   10.1029/2000jd900772, 2001.

874   Pusede, S. E., Steiner, A. L., and Cohen, R. C.: Temperature and Recent Trends in the Chemistry

875   of Continental Surface Ozone, Chemical Reviews, 115, 3898-3918, 10.1021/cr5006815, 2015.

876   Qu, Z., Henze, D. K., Capps, S. L., Wang, Y., Xu, X., Wang, J., and Keller, M.: Monthly top-down

877   NOx emissions for China (2005–2012): A hybrid inversion method and trend analysis, Journal of

878   Geophysical Research: Atmospheres, 122, 4600-4625, https://doi.org/10.1002/2016JD025852,

879   2017.

880   Qu, Z., Henze, D. K., Li, C., Theys, N., Wang, Y., Wang, J., Wang, W., Han, J., Shim, C.,

881   Dickerson, R. R., and Ren, X.: SO2 Emission Estimates Using OMI SO2 Retrievals for 2005-2017,

882   J Geophys Res Atmos, 124, 8336-8359, 10.1029/2019JD030243, 2019.

883   Sha, T., Ma, X. Y., Zhang, H. X., Janechek, N., Wang, Y. Y., Wang, Y., Garcia, L. C., Jenerette,

884   G. D., and Wang, J.: Impacts of Soil NOx Emission on O-3 Air Quality in Rural California,

885   Environmental Science & Technology, 55, 7113-7122, 10.1021/acs.est.0c06834, 2021.

Shi, X. and Brasseur, G. P.: The Response in Air Quality to the Reduction of Chinese Economic Activities During the COVID-19 Outbreak, Geophys Res Lett, 47, 10.1029/2020gl088070, 2020.

Sillman, S., Logan, J. A., and Wofsy, S. C.: The sensitivity of ozone to nitrogen-oxides and hydrocarbons in regional ozone episodes, Journal of Geophysical Research-Atmospheres, 95, 1837-1851, 10.1029/JD095iD02p01837, 1990.

Steinbacher, M., Zellweger, C., Schwarzenbach, B., Bugmann, S., Buchmann, B., Ordóñez, C., Prevot, A. S. H., and Hueglin, C.: Nitrogen oxide measurements at rural sites in Switzerland: Bias of conventional measurement techniques, Journal of Geophysical Research: Atmospheres, 112, https://doi.org/10.1029/2006JD007971, 2007.

Streets, D. G., Canty, T., Carmichael, G. R., de Foy, B., Dickerson, R. R., Duncan, B. N., Edwards, D. P., Haynes, J. A., Henze, D. K., Houyoux, M. R., Jacob, D. J., Krotkov, N. A., Lamsal, L. N., Liu, Y., Lu, Z., Martin, R. V., Pfister, G. G., Pinder, R. W., Salawitch, R. J., and Wecht, K. J.: Emissions estimation from satellite retrievals: A review of current capability, Atmospheric Environment, 77, 1011-1042, 10.1016/j.atmosenv.2013.05.051, 2013.

Sun, K., Zhu, L., Cady-Pereira, K., Chan Miller, C., Chance, K., Clarisse, L., Coheur, P.-F., González Abad, G., Huang, G., Liu, X., Van Damme, M., Yang, K., and Zondlo, M.: A physics-based approach to oversample multi-satellite, multispecies observations to a common grid, Atmospheric Measurement Techniques, 11, 6679-6701, 10.5194/amt-11-6679-2018, 2018.

Tong, L., Liu, Y., Meng, Y., Dai, X. R., Huang, L. J., Luo, W. X., Yang, M. R., Pan, Y., Zheng, J., and Xiao, H.: Surface ozone changes during the COVID-19 outbreak in China: An insight into the pollution characteristics and formation regimes of ozone in the cold season, Journal of Atmospheric Chemistry, 80, 103-120, 10.1007/s10874-022-09443-2, 2023.

Travis, K. R., Jacob, D. J., Keller, C. A., Kuang, S., Lin, J., Newchurch, M. J., and Thompson, A. M.: Resolving ozone vertical gradients in air quality models, Atmos. Chem. Phys. Discuss., 2017, 1-18, 10.5194/acp-2017-596, 2017.

Travis, K. R., Jacob, D. J., Fisher, J. A., Kim, P. S., Marais, E. A., Zhu, L., Yu, K., Miller, C. C., Yantosca, R. M., Sulprizio, M. P., Thompson, A. M., Wennberg, P. O., Crounse, J. D., St Clair, J. M., Cohen, R. C., Laughner, J. L., Dibb, J. E., Hall, S. R., Ullmann, K., Wolfe, G. M., Pollack, I. B., Peischl, J., Neuman, J. A., and Zhou, X.: Why do Models Overestimate Surface Ozone in the Southeastern United States?, Atmos Chem Phys, 16, 13561-13577, 10.5194/acp-16-13561-2016, 2016.

917 van der Werf, G. R., Randerson, J. T., Giglio, L., van Leeuwen, T. T., Chen, Y., Rogers, B. M.,
918 Mu, M., van Marle, M. J. E., Morton, D. C., Collatz, G. J., Yokelson, R. J., and Kasibhatla, P. S.:
919 Global fire emissions estimates during 1997–2016, Earth System Science Data, 9, 697-720,
920 10.5194/essd-9-697-2017, 2017.

921 TROPOMI ATBD of the total and tropospheric NO2 data products:
922 https://sentinel.esa.int/documents/247904/2476257/sentinel-5p-tropomi-atbd-no2-data-products,
923 last access: Sep. 29.

924 van Geffen, J., Boersma, K. F., Eskes, H., Sneep, M., ter Linden, M., Zara, M., and Veefkind, J.
925 P.: S5P TROPOMI NO2 slant column retrieval: method, stability, uncertainties and comparisons
926 with OMI, Atmospheric Measurement Techniques, 13, 1315-1335, 10.5194/amt-13-1315-2020,
927 2020.

928 Veefkind, J. P., Aben, I., McMullan, K., Förster, H., de Vries, J., Otter, G., Claas, J., Eskes, H. J.,
929 de Haan, J. F., Kleipool, Q., van Weele, M., Hasekamp, O., Hoogeveen, R., Landgraf, J., Snel, R.,
930 Tol, P., Ingmann, P., Voors, R., Kruizinga, B., Vink, R., Visser, H., and Levelt, P. F.: TROPOMI
931 on the ESA Sentinel-5 Precursor: A GMES mission for global observations of the atmospheric
932 composition for climate, air quality and ozone layer applications, Remote Sensing of Environment,
933 120, 70-83, https://doi.org/10.1016/j.rse.2011.09.027, 2012.

934 Venter, Z. S., Aunan, K., Chowdhury, S., and Lelieveld, J.: COVID-19 lockdowns cause global
935 air pollution declines, Proceedings of the National Academy of Sciences, 117, 18984-18990,
936 doi:10.1073/pnas.2006853117, 2020.

937 Verhoelst, T., Compernolle, S., Pinardi, G., Lambert, J. C., Eskes, H. J., Eichmann, K. U., Fjæraa,
938 A. M., Granville, J., Niemeijer, S., Cede, A., Tiefengraber, M., Hendrick, F., Pazmiño, A., Bais,
939 A., Bazureau, A., Boersma, K. F., Bognar, K., Dehn, A., Donner, S., Elokhov, A., Gebetsberger,
940 M., Goutail, F., de la Mora, M. G., Gruzdev, A., Gratsea, M., Hansen, G. H., Irie, H., Jepsen, N.,
941 Kanaya, Y., Karagkiozidis, D., Kivi, R., Kreher, K., Levelt, P. F., Liu, C., Müller, M., Comas, M.
942 N., Piters, A. J. M., Pommereau, J. P., Portafaix, T., Prados-Roman, C., Puentedura, O., Querel,
943 R., Remmers, J., Richter, A., Rimmer, J., Cárdenas, C. R., de Miguel, L. S., Sinyakov, V. P.,
944 Stremme, W., Strong, K., Van Roozendael, M., Veefkind, J. P., Wagner, T., Wittrock, F., González,
945 M. Y., and Zehner, C.: Ground-based validation of the Copernicus Sentinel-5P TROPOMI NO2
946 measurements with the NDACC ZSL-DOAS, MAX-DOAS and Pandonia global networks,
947 Atmospheric Measurement Techniques, 14, 481-510, 10.5194/amt-14-481-2021, 2021.

Vigouroux, C., Langerock, B., Aquino, C. A. B., Blumenstock, T., Cheng, Z. B., De Mazière, M., De Smedt, I., Grutter, M., Hannigan, J. W., Jones, N., Kivi, R., Loyola, D., Lutsch, E., Mahieu, E., Makarova, M., Metzger, J. M., Morino, I., Murata, I., Nagahama, T., Notholt, J., Ortega, I., Palm, M., Pinardi, G., Röhling, A., Smale, D., Stremme, W., Strong, K., Sussmann, R., Té, Y., van Roozendael, M., Wang, P. C., and Winkler, H.: TROPOMI-Sentinel-5 Precursor formaldehyde validation using an extensive network of ground-based Fourier-transform infrared stations, Atmospheric Measurement Techniques, 13, 3751-3767, 10.5194/amt-13-3751-2020, 2020.

Vinken, G. C. M., Boersma, K. F., van Donkelaar, A., and Zhang, L.: Constraints on ship NOx emissions in Europe using GEOS-Chem and OMI satellite NO2 observations, Atmos. Chem. Phys., 14, 1353-1369, 10.5194/acp-14-1353-2014, 2014.

Wang, Y., Wang, J., Xu, X., Henze, D. K., Qu, Z., and Yang, K.: Inverse modeling of SO_2 and NO_x emissions over China using multisensor satellite data – Part 1: Formulation and sensitivity analysis, Atmospheric Chemistry and Physics, 20, 6631-6650, 10.5194/acp-20-6631-2020, 2020a.

Wang, Y., Wang, J., Zhou, M., Henze, D. K., Ge, C., and Wang, W.: Inverse modeling of SO_2 and NO_x emissions over China using multisensor satellite data – Part 2: Downscaling techniques for air quality analysis and forecasts, Atmospheric Chemistry and Physics, 20, 6651-6670, 10.5194/acp-20-6651-2020, 2020b.

Wang, Y. X., McElroy, M. B., Jacob, D. J., and Yantosca, R. M.: A nested grid formulation for chemical transport over Asia: Applications to CO, Journal of Geophysical Research: Atmospheres, 109, n/a-n/a, 10.1029/2004jd005237, 2004.

Williams, J. and Koppmann, R.: Volatile Organic Compounds in the Atmosphere: An Overview, in: Volatile Organic Compounds in the Atmosphere, 1-32, https://doi.org/10.1002/9780470988657.ch1, 2007.

Zhang, L., Jacob, D. J., Knipping, E. M., Kumar, N., Munger, J. W., Carouge, C. C., van Donkelaar, A., Wang, Y. X., and Chen, D.: Nitrogen deposition to the United States: distribution, sources, and processes, Atmospheric Chemistry and Physics, 12, 4539-4554, 10.5194/acp-12-4539-2012, 2012.

Zhang, Q., Pan, Y., He, Y., Walters, W. W., Ni, Q., Liu, X., Xu, G., Shao, J., and Jiang, C.: Substantial nitrogen oxides emission reduction from China due to COVID-19 and its impact on surface ozone and aerosol pollution, Science of The Total Environment, 753, 10.1016/j.scitotenv.2020.142238, 2021.

978   Zhang, R. X., Zhang, Y. Z., Lin, H. P., Feng, X., Fu, T. M., and Wang, Y. H.: NOx Emission
979   Reduction and Recovery during COVID-19 in East China, Atmosphere, 11,
980   10.3390/atmos11040433, 2020.

981   Zhang, Y.-L. and Cao, F.: Fine particulate matter (PM2.5) in China at a city level, Scientific
982   Reports, 5, 14884, 10.1038/srep14884, 2015.

983   Zhao, Y., Zhang, K., Xu, X., Shen, H., Zhu, X., Zhang, Y., Hu, Y., and Shen, G.: Substantial
984   Changes in Nitrogen Dioxide and Ozone after Excluding Meteorological Impacts during the
985   COVID-19 Outbreak in Mainland China, Environmental Science & Technology Letters, 7, 402-
986   408, 10.1021/acs.estlett.0c00304, 2020.

987   Zheng, B., Tong, D., Li, M., Liu, F., Hong, C., Geng, G., Li, H., Li, X., Peng, L., Qi, J., Yan, L.,
988   Zhang, Y., Zhao, H., Zheng, Y., He, K., and Zhang, Q.: Trends in China's anthropogenic emissions
989   since 2010 as the consequence of clean air actions, Atmospheric Chemistry and Physics, 18,
990   14095-14111, 10.5194/acp-18-14095-2018, 2018.

991